Materials Advances

PAPER

View Article Online
View Journal

Cite this: DOI: 10.1039/d5ma01472g

A high-capacity 2.5 V aqueous K^+/Zn^{2+} mixed ions hybrid supercapacitor enabled by an electrochemically pre-intercalated α-MnO_2/carbon black cathode

Raghupathy Rajesh [ab] and Annamalai Senthil Kumar *[ab]

Due to their inherent safety and environmental sustainability, aqueous zinc-ion hybrid supercapacitors (AZIHCs) continue to attract significant research attention. Among various cathode materials, manganese dioxide (MnO_2) stands out for its low cost and low toxicity. However, challenges such as limited operating voltage, poor cycling stability, and low energy density hinder its broader application. In this work, an α-MnO_2 functionalized low-cost carbon black composite, denoted as CB-MnO_2@Zn, is synthesized *via* a simple co-precipitation method followed by electrochemical Zn^{2+} modification, as a high-performance cathode material for efficient Zn^{2+} intercalation/deintercalation reaction. The composite was evaluated for both supercapacitor and aqueous Zn^{2+}/K^+ hybrid ions battery applications in a dilute 1 mM Zn^{2+} solution containing 0.1 M KCl (optimal). Comprehensive physicochemical (XRD, XPS, FTIR, and Raman) and electrochemical (*operando* EQCM and SECM) characterization methods confirmed the highly redox-active nature of the material, enabling highly reversible Zn^{2+} intercalation/deintercalation with minimal Mn^{2+} dissolution. The carbon black matrix effectively accommodates volume changes during cycling, thereby maintaining structural integrity and enhancing electrochemical stability. Formation of zinc hydroxy-sulphate (ZHS, $M_w \sim 416$ g mol^{-1}) and $Zn^{2+}/Zn(OH)_2$-like intermediate species was identified and visualized. The CB–MnO_2@Zn composite exhibited an outstanding specific capacitance of 811.6 F g^{-1} at 1 A g^{-1}, corresponding to an energy density of 162.3 Wh kg^{-1}. Remarkably, it retained excellent capacitance and >95% efficiency over 5000 cycles. The assembled Zn^{2+}/K^+ hybrid battery (Zn‖CB–MnO_2@Zn) demonstrated a specific capacity of 315 mAh g^{-1} at 0.25 A g^{-1}, a high energy density of 273.45 Wh kg^{-1}, and a power density of 1844.4 W kg^{-1}. Moreover, the battery exhibited superior rate capability and retained 94% capacity and 99% coulombic efficiency after 5000 cycles, highlighting its potential for durable and high-energy aqueous energy storage systems.

Received 16th December 2025,
Accepted 6th March 2026

DOI: 10.1039/d5ma01472g

rsc.li/materials-advances

Open Access Article. Published on 11 May 2026. Downloaded on 6/1/2026 10:54:30 PM.
This article is licensed under a Creative Commons Attribution-NonCommercial 3.0 Unported Licence.

1. Introduction

The growing global demand for safe, sustainable, and economically viable energy-storage systems (ESSs) has intensified the search for next-generation technologies capable of meeting diverse operational requirements.[1,2] Conventional ESSs such as metal-ion batteries, metal–oxygen batteries, supercapacitors, and lithium-ion batteries (LIBs) have been widely developed and deployed. Among these, LIBs continue to dominate modern storage markets; however, their long-term scalability is restricted by several inherent limitations. Key concerns include safety risks associated with flammable organic electrolytes and thermal runaway, as well as resource scarcity and ethical issues linked to lithium, nickel, and cobalt extraction.[3,4] Although LIBs provide high energy densities (150–250 Wh kg^{-1}), their power density (~200–2000 W kg^{-1}), slow charging rate (~2 h), and moderate cycle life (~2000 cycles) remain insufficient for applications requiring both rapid power delivery and extended energy buffering, such as electric vehicles (EVs), regenerative braking, renewable-energy smoothing, and grid ancillary services. Many practical systems require short bursts of high power alongside sustained energy storage, a dual demand that is difficult for LIBs alone to satisfy.[5,6] In contrast, supercapacitors offer exceptionally high-power density (~10 000 W kg^{-1}), ultrafast charging (seconds), and long cycle life (>100 000 cycles), but their limited energy density severely

---

[a] Nano and Bioelectrochemistry Research Laboratory, CO_2 Research and Green Technologies Centre, Vellore Institute of Technology, India. E-mail: askumarchem@yahoo.com, askumar@vit.ac.in; Tel: +91-416-2202754
[b] Department of Chemistry, School of Advanced Sciences, Vellore Institute of Technology University, Vellore, 632 014, Tamil Nadu, India

© 2026 The Author(s). Published by the Royal Society of Chemistry

Open Access Article. Published on 11 May 2026. Downloaded on 6/1/2026 10:54:30 PM.
This article is licensed under a Creative Commons Attribution-NonCommercial 3.0 Unported Licence.

restricts their use as stand-alone storage solutions.[7] Hybrid energy-storage systems (HESSs), which integrate a battery with a supercapacitor, have emerged as an effective solution to meet both high-power and high-energy requirements. In HESS devices, the supercapacitor handles transient high-power events and protects the battery from extreme current loads, thereby improving overall efficiency, extending battery life, and enabling operation closer to the battery's optimal regime.[8,9]

The concept of hybrid storage was first demonstrated by Amatucci *et al.* in 2001, who introduced a nonaqueous lithium-ion capacitor composed of an activated-carbon positive electrode (storing charge *via* non-faradaic or pseudocapacitive anion adsorption) and a nanostructured $Li_4Ti_5O_{12}$ negative electrode operating through fast, reversible lithium intercalation.[10] Although this system delivered a wide voltage window (3.0–3.5 V) and a power density of ~20 Wh kg^{-1}, it suffered from several intrinsic drawbacks. The use of flammable organic electrolytes imposes safety hazards and manufacturing complexity, while mandatory pre-lithiation increases cost and moisture sensitivity.[11] Moreover, such devices exhibit lower ionic conductivity, narrow temperature tolerance, and shorter cycle life compared with aqueous hybrid systems and carbon-based supercapacitors.[12,13]

Aqueous hybrid supercapacitors (AHCs) have therefore emerged as a promising alternative, combining high safety, fast ion transport, environmental compatibility, and low cost. Their inherently high ionic conductivity (~1 S cm^{-1}) enables rapid charge–discharge kinetics and high power output, while the combination of battery-type faradaic electrodes with capacitive/pseudocapacitive materials enhances energy density beyond conventional electrical double-layer capacitors (EDLCs).[14] AHCs are thus attractive for wearable electronics, portable devices, transportation systems, and grid-scale applications.[15] Among all AHC systems, aqueous Zn-ion hybrid supercapacitors (AZHCs) offer the most favorable balance of energy density (80–150 Wh kg^{-1}), power density (5000–20 000 W kg^{-1}), safety, long cycle life, and low material cost.[16–18] The Zn metal anode provides a high theoretical capacity (820 mAh g^{-1}) and stable two-electron faradaic redox behavior, enabling higher voltages (1.2–1.9 V) and greater energy storage than most aqueous asymmetric devices.[19,20] The combination of fast Zn^{2+} transport in aqueous media with capacitive or pseudocapacitive cathodes enables AZHCs to deliver supercapacitor-level power while retaining battery-like energy characteristics.[21,22] Their reliance on earth-abundant materials, nonflammable electrolytes, and structurally robust electrode chemistries makes them compelling candidates for next-generation aqueous ESSs.[23,24]

Despite these merits, AZHCs face several challenges. The Zn anode is prone to dendritic growth, hydrogen evolution, and surface passivation, which compromise reversibility and coulombic efficiency.[25] The narrow electrochemical stability window of water (1.3–1.7 V) limits maximum voltage and energy density.[26] On the cathode side, the materials used suffer dissolution, irreversible phase transitions, and sluggish Zn^{2+} diffusion due to strong electrostatic interactions.[27] Electrolyte pH fluctuations, temperature sensitivity, and mass-loading constraints further hinder practical implementation.[28] Overcoming these limitations requires electrolyte engineering, interface modification, structural stabilization, and advanced composite cathode design.[29,30]

MnO_2-based cathodes are particularly attractive for AZHCs because of their pseudocapacitive surface redox activity, tunable layered/tunnel structures that facilitate Zn^{2+} intercalation, low cost, abundance, and excellent compatibility with mild aqueous Zn electrolytes.[12,13] Layered δ-MnO_2, tunnel α-MnO_2, and MnO_2/carbon or MnO_2/MXene composites are widely studied for their high theoretical capacity, multiple fast redox pathways (Zn^{2+}/H^+ insertion coupled with surface pseudocapacitance), and scalable synthesis.[24,31–33] Carbon black (CB) is a conductive carbonaceous material with high surface area and excellent electrical conductivity, widely employed as a conductive additive in electrochemical systems to enhance electron transport and improve overall electrode performance.[34,35] However, MnO_2 suffers from intrinsic limitations including Mn dissolution, irreversible structural collapse under deep Zn^{2+}/H^+ insertion, low electronic conductivity, and sensitivity to electrolyte composition. Accordingly, current research focuses on stabilizing MnO_2 *via* pre-intercalation (K^+ and Zn^{2+}), defect/doping strategies, conductive frameworks, electrolyte additives, and nanoscale morphology control to achieve durable, high-voltage (~2.0 V) aqueous Zn-ion hybrid devices.[36–38] MnO_2-based AZHCs typically employ three electrolyte strategies: (i) Zn^{2+}-only electrolytes (*e.g.*, 1–2 M $ZnSO_4$, $Zn(OTf)_2$, and $Zn(Ac)_2$), which offer high ionic conductivity and reversible Zn plating/stripping but suffer from Mn dissolution, HER, and structural degradation;[39–41] (ii) K^+-stabilized MnO_2 systems, where K^+ pre-intercalation enlarges interlayer spacing, enhances Zn^{2+} diffusion, and improves stability without serving as the primary charge carrier;[23,42] (iii) mixed K^+/Zn^{2+} dual-cation electrolytes, where K^+ stabilizes the MnO_2 framework and accelerates ion transport, while Zn^{2+} provides high faradaic capacity. Such dual-cation electrolytes enable higher working voltages (~1.8–2.2 V), improved cycling stability, and suppressed Mn dissolution, but require careful optimization to prevent competing ion-insertion reactions and pH imbalance. Overall, Zn^{2+} electrolytes provide high capacity, K^+ pre-intercalation enhances MnO_2 structural integrity, and mixed K^+/Zn^{2+} electrolytes offer the optimal synergy of energy, stability, and voltage for high-performance MnO_2-based aqueous Zn-ion hybrids.[43–45]

In general, the preparation of pre-intercalated MnO_2 matrices is commonly carried out using autoclave-assisted (hydrothermal) methods, as reported in several studies.[36,38,39] For example, in 2020, Chen *et al.* synthesized Zn–MnO_2 anchored on carbon cloth (2 cm × 3 cm) *via* a one-pot hydrothermal process using $KMnO_4$, $Zn(NO_3)_2 \cdot 6H_2O$, and carbon cloth as precursors. However, hydrothermal routes often suffer from poor control over the stoichiometry and spatial uniformity of Zn pre-intercalation within the MnO_2 structure, leading to batch-to-batch variability and inconsistent electrochemical performance.[36] In this work, we introduce a K/Zn ions pre-intercalated α-MnO_2/carbon black composite

© 2026 The Author(s). Published by the Royal Society of Chemistry

Open Access Article. Published on 11 May 2026. Downloaded on 6/1/2026 10:54:30 PM.
This article is licensed under a Creative Commons Attribution-NonCommercial 3.0 Unported Licence.

(CB–MnO$_2$@Zn), synthesized through a two-step, highly controlled procedure involving bulk precipitation followed by electrochemical Zn^{2+} intercalation. This strategy enables precise tuning of Zn incorporation and ensures structural uniformity, resulting in an advanced and reproducible cathode material for high-voltage aqueous K$^+$/Zn^{2+} hybrid supercapacitors (AKZHCs). Using an optimized mixed-ions electrolyte (0.1 M K$^+$ and 1 mM Zn^{2+}), the device achieves a remarkably high operating voltage of 2.5 V without requiring Mn^{2+} additives. The composite exhibits excellent supercapacitor performance, delivering 811.6 F g^{-1} at 1 A g^{-1}, corresponding to 162.3 Wh kg^{-1}, far exceeding typical MnO$_2$/carbon systems (200–500 F g^{-1}). A full Zn‖CB–MnO$_2$@Zn cell delivers a discharge capacity of 315 mAh g^{-1}, an energy density of 273.45 Wh kg^{-1}, and a power density of 1844.4 W kg^{-1}, with 99% coulombic efficiency and 94% capacity retention over 5000 cycles, significantly outperforming state-of-the-art AZIBs. *In situ* EQCM analysis further reveals the formation of a Zn hydroxide sulfate (ZHS) intermediate (molecular mass: 414.5 g mol^{-1}), elucidating the underlying Zn^{2+} intercalation mechanism. This work demonstrates a cost-effective MnO$_2$-based composite and a finely tuned mixed-ions electrolyte capable of supporting high-voltage aqueous Zn/K-ions hybrid energy storage, offering a promising pathway toward advanced, safe, and scalable battery–supercapacitor hybrid technologies.

2. Experimental section

2.1. Chemicals and reagents

Carbon black (N330 grade) was kindly provided as a gift sample by Phillips Carbon Black Ltd, Kochi, India. Potassium permanganate (KMnO$_4$; ≥99%, analytical grade) and zinc sulfate heptahydrate (ZnSO$_4$·7H$_2$O; ≥99%, analytical grade) were purchased from Sigma-Aldrich, and all other chemicals used were of analytical grade and used without further purification. Aqueous solutions were prepared using deionized water and double-distilled water (DDW) pre-treated with alkaline KMnO$_4$ where required. A 0.1 M KCl solution at neutral pH (pH 7) was employed as the supporting electrolyte.

2.2. Synthesis of a CB–MnO$_2$ nanocomposite

100 mg of CB was dispersed in 50 mL of a 1 : 1 (v/v) mixture of deionized water and ethanol, followed by magnetic stirring for 5 minutes. Subsequently, 10 mL of 0.1 M KMnO$_4$ solution was added, and the mixture was stirred continuously for 2 hours. After this, 10 mL of 30% H$_2$O$_2$ was added dropwise under constant stirring, and the reaction was allowed to proceed for an additional hour. The resulting precipitate was collected, thoroughly washed several times with ethanol and hexane to remove impurities and dried at 40 °C to obtain the CB–α-MnO$_2$ nanocomposite (SI Scheme S1).

2.3. Working electrode preparation

A pre-anodized graphite paper (GP) was employed as the current collector. The fresh GP electrode was kept at 2 V *vs.* Ag/AgCl for 3 minutes to activate the surface functional groups. The synthesized carbon black–manganese dioxide (CB–MnO$_2$) composite was dispersed in ethanol and sonicated for approximately 20 minutes to form a homogeneous suspension. This suspension was then drop-cast onto a 1 cm^2 area of the GP surface. After casting, the electrode was air-dried under ambient conditions for a few minutes to allow solvent evaporation and ensure proper adhesion of the active material. To quantify the active material loading, the electrode was weighed before and after the coating process. The difference in mass corresponded to the amount of CB–MnO$_2$ deposited on the GP, which was approximately 1 mg cm^{-2}, and it is denoted as GP/CB–MnO$_2$. The loading value used in this work is like several of previous literature reports.[36,38]

2.4. *In Situ* synthesis of CB–MnO$_2$@Zn

The CB–MnO$_2$@Zn electrode was prepared following the same procedure described in Section 2.3. The resulting GP/CB–MnO$_2$ electrode was then subjected to ten consecutive cyclic voltammetry cycles within a potential window of −0.2 to 1.0 V *vs.* Ag/AgCl, at a scan rate of 5 mV s^{-1}, using an electrolyte composed of 1 mM ZnSO$_4$ and 0.1 M KCl. After the electrochemical treatment, the modified electrode was gently rinsed with distilled water to remove any loosely adsorbed ionic species and was subsequently used for further energy applications. This electrode is hereafter referred to as GP/CB–MnO$_2$@Zn. In the electrochemical process, Zn(OH)$_2$ like species were electrochemically deposited onto the surface, exhibiting good mechanical stability and functioning as a binder for the underlying electrode material.

2.5. Micro-pouch cell battery assembly

A micro-scale pouch cell was assembled using a Zn wire (∼1 mm diameter, 4 cm long) as the anode and a GP/CB–MnO$_2$@Zn composite as the cathode. The electrolyte comprised an aqueous solution containing 0.1 M KCl and 1 mM ZnSO$_4$. Whatman GF/A glass fibre filter paper was employed as the separator owing to its high ionic conductivity and excellent mechanical stability. During cell assembly, the Zn wire anode and the cathode were positioned in parallel, separated by the electrolyte-soaked GF/A separator. The components were then stacked and encapsulated within an inert, flexible polyethylene film, which was sealed using a heat sealer to form a compact micro-pouch cell. The assembled cell was allowed to rest for 5 minutes prior to electrochemical measurements to ensure equilibrium at the electrode–electrolyte interfaces (illustration of a battery, Scheme 1A).

2.6. Materials and methods – instrumentation and electrochemical measurements

The X-ray diffraction (XRD) pattern was recorded using a Bruker AXS D8 Focus Advanced X-ray diffractometer (Rigaku, Tokyo, Japan). Fourier-transform infrared (FTIR) spectroscopy was performed using a Shimadzu IR Affinity-1 spectrometer. Raman spectra were obtained using a RENISHAW InVia Laser Raman microscope equipped with a He–Ne laser source (λ = 633 nm).

Open Access Article. Published on 11 May 2026. Downloaded on 6/1/2026 10:54:30 PM.
This article is licensed under a Creative Commons Attribution-NonCommercial 3.0 Unported Licence.

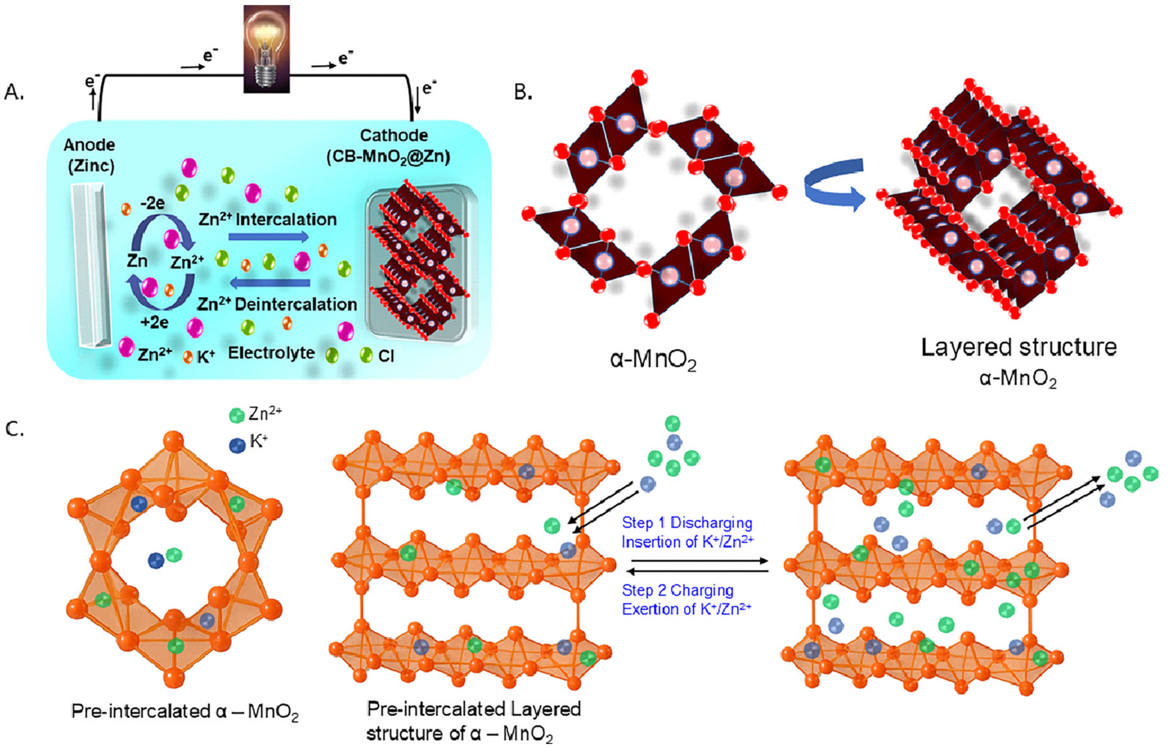

Scheme 1 Systematic illustration of a Zn‖CB–MnO_2@Zn unit based aqueous Zn/K ions hybrid supercapacitor-battery (A). Crystal structure of α-MnO_2. (B). Typical illustration of the insertion and exertion of K^+/Zn^{2+} ions in the tunnel structure of α-MnO_2 during discharge and charge mechanisms.

Field emission scanning electron microscopy (FESEM) analysis was carried out using an FEI Quanta microscope (Thermo Fisher Scientific). X-ray photoelectron spectroscopy (XPS) was conducted using a Kratos Axis Ultra DLD spectrometer (UK) with a monochromatic Al Kα radiation source (photon energy = 1486.6 eV, resolution = 0.35 eV). All binding energy (BE) values were calibrated using the C 1s peak at 284.6 eV as a reference. Deconvolution of individual XPS peaks was performed using XPSPEAK 4.1 software.

Electrochemical measurements, including cyclic voltammetry and galvanostatic charge–discharge (GCD), were performed using a Biologic SP-200 electrochemical workstation (USA). A three-electrode setup was employed, consisting of a graphite paper (GP; working area, 1 cm^2) as the working electrode, Ag/AgCl as the reference electrode, and a platinum wire as the counter electrode, using 0.1 M KCl aqueous solution as the electrolyte. For two-electrode measurements, the configuration included a GPs (1 cm^2) as the cathode (current collector) and a zinc wire (working area ~1.5 mm diameter × 10 mm length) as the anode. Electrochemical impedance spectroscopy (EIS) was conducted using 5 mM $[Fe(CN)_6]^{3-}$ dissolved in 0.1 M KCl at a bias potential of 0.2 V *vs.* Ag/AgCl. Scanning electrochemical microscopy (SECM) experiments were carried out using a Princeton applied research (PAR) Versascan bipotentiostat. A glassy carbon electrode (GCE) with a geometric area of 0.0707 cm^2 (3 mm diameter) served as the substrate, while a 25 μm platinum ultramicroelectrode tip was used under bipotentiostatic control. The positioning of the Pt tip relative to the modified substrate was optimized using approach curves in the tip-generation/substrate-collection (TG/SC) mode by advancing the tip at 2 μm s^{-1} along the *z*-axis. During analysis, the Pt tip was biased at −0.25 V *vs.* Ag/AgCl, and the substrate was held at open circuit potential to facilitate TG/SC-based redox cycling.

In situ cyclic voltammetry–electrochemical quartz crystal microbalance (CV–EQCM) measurements were conducted using a gold-coated quartz crystal electrode (EQCM-Au) with a geometric surface area of 0.196 cm^2.

3. Results and discussion

3.1. Physicochemical characterization of the synthesized CB–MnO_2@Zn nanocomposite

The crystalline phases of the as-prepared samples were confirmed by XRD, as shown in Fig. 1A. The broad featureless pattern of carbon black (CB, curve *a*) indicates its amorphous nature with only a weak reflection at ~25° corresponding to graphitic (002) planes. Pure MnO_2 (curve *b*) exhibits sharp diffraction peaks that can be indexed to the α-MnO_2 phase (JCPDS No. 44-0141), confirming its high crystallinity. The characteristic reflections at (200), (310), (211), (301), (411), and (521) planes match well with the tetragonal tunnel-type α-MnO_2 structure (SI, Fig. S1). For the CB–MnO_2 composite (curve *c*), the diffraction peaks of α-MnO_2 are retained without additional impurity phases, though with relatively reduced intensity and slight peak broadening, suggesting successful

© 2026 The Author(s). Published by the Royal Society of Chemistry

Open Access Article. Published on 11 May 2026. Downloaded on 6/1/2026 10:54:30 PM.
This article is licensed under a Creative Commons Attribution-NonCommercial 3.0 Unported Licence.

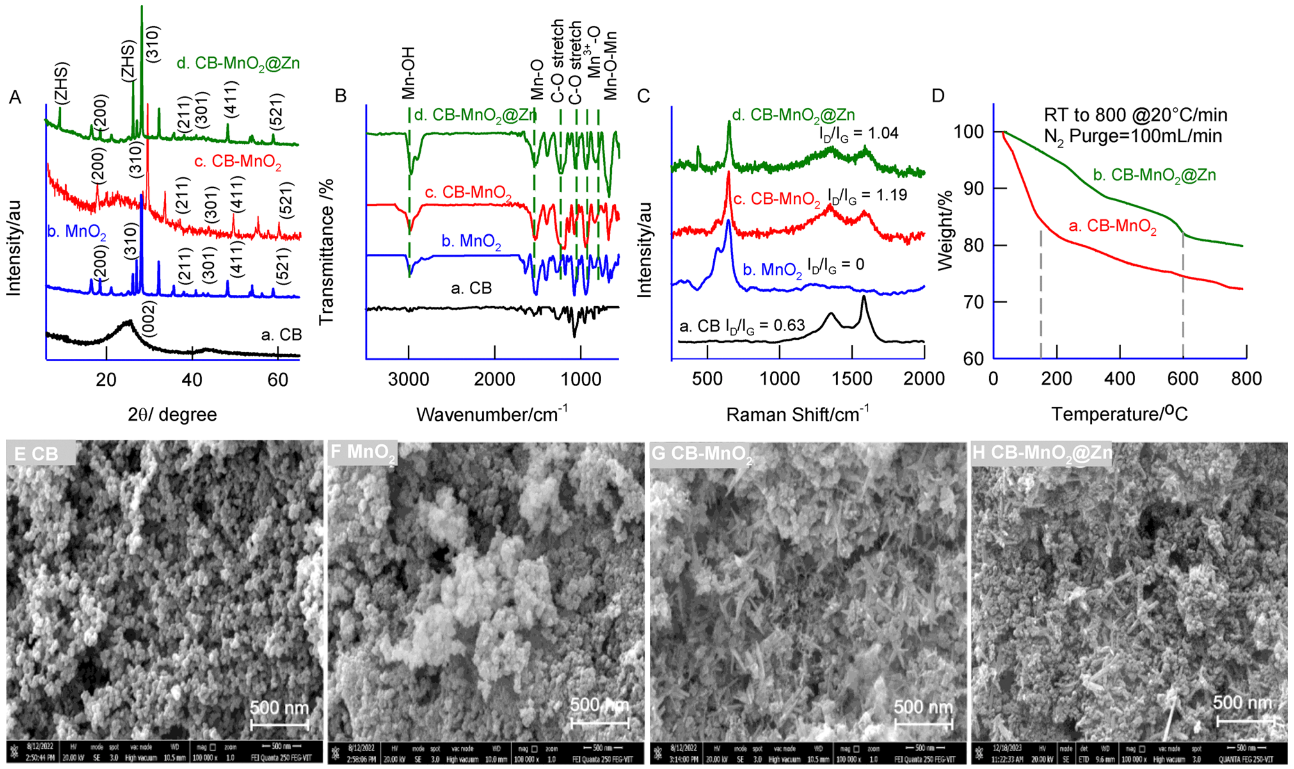

Fig. 1 (A) XRD, (B) FTIR and (C) Raman and (D) TGA characterization analyses of CB (curve a), MnO$_2$ (curve b), CB–MnO$_2$ (curve c) and CB–MnO$_2$@Zn (curve d). FESEM images of (E) CB, (B) MnO$_2$, (C) CB–MnO$_2$ and (D) CB–MnO$_2$@Zn.

dispersion of MnO$_2$ nanoparticles on the CB matrix with partial reduction in crystallite size. Importantly, the CB background persists, verifying the hybrid nature of the composite. In the case of Zn-intercalated CB–MnO$_2$ (curve d), additional diffraction peaks corresponding to zinc hydroxide sulfate hydrate[44–47] (ZHS, JCPDS No. 39-0688) are clearly observed along with α-MnO$_2$ reflections (SI, Fig. S1). This indicates partial Zn^{2+} intercalation/precipitation during cycling, which may serve as a structural stabilizer.[48,49] The coexistence of MnO$_2$ and ZHS phases confirms successful Zn modification of the CB–MnO$_2$@Zn composite.

Fig. 1B shows the FTIR spectra of the samples. CB (curve a) displays characteristic stretching vibrations at 1276 cm^{-1} and 1089 cm^{-1}, corresponding to C–O stretching. α-MnO$_2$ (curve b) shows peaks at 2989 cm^{-1} (Mn–OH stretching), 1546 cm^{-1} and 1406 cm^{-1} (Mn–O stretching), 949 cm^{-1} (Mn^{3+}–O stretching), and 679 cm^{-1} (Mn–O stretching), indicative of the Mn–O–Mn framework.[50] The FTIR spectrum of the CB–MnO$_2$ nanocomposite exhibits a combination of the characteristic peaks of both CB and MnO$_2$, confirming the successful integration of MnO$_2$ onto the CB surface (Fig. 1b, curve c). FT-IR spectroscopy (Fig. 1B, curve d) further confirmed the incorporation of Zn^{2+} into the composite matrix. A distinct absorption band observed at 683 cm^{-1} is attributed to the Zn–O stretching vibration.[51] This band overlaps with the characteristic Mn–O–Mn bridging vibrations, resulting in an intensified and broadened peak. The enhanced absorption in this region provides strong evidence for the *in situ* formation of ZnO like species within the MnO$_2$ framework, indicating successful Zn^{2+} integration and interaction with the host matrix.

To further support the composite formation, Raman spectroscopy was performed (Fig. 1C). Curve a represents pristine CB, exhibiting prominent disordered graphitic (D, sp^3 sites) and ordered graphitic (G, sp^2 sites) bands at 1354 and 1596 cm^{-1} respectively.[52] These bands are absent in the pure MnO$_2$ spectrum (Fig. 1C, curve b), which instead shows its distinct Raman features at 660, 550 and about 480 cm^{-1} due to symmetric stretching vibration of the Mn–O bonds within the MnO$_6$ octahedra, Mn–O–Mn deformation modes or other Mn–O stretching vibrations and skeletal vibrations of MnO$_2$ respectively.[53–55] In the CB@MnO$_2$ composite (Fig. 1C, curve c), the D and G bands of CB are retained along with the characteristic peaks of MnO$_2$. Notably, the intensity ratio of the D to G bands (I_D/I_G) increases from 0.63 in CB to 1.19 in the CB@MnO$_2$ nanocomposite along with 9–19 cm^{-1} shift in the frequencies (see SI Table S1). The increase in I_D/I_G indicates structural interaction of sp^2 bonds of CB with Mn–O functional groups with increased defect structure. The intimate physical contact between MnO$_2$ and CB is likely to induce lattice strain within the graphitic sites of the carbon matrix, thereby modifying its vibrational characteristics. The close spatial proximity of carbon can alter the local electronic environment surrounding the MnO$_6$ octahedra, leading to noticeable shifts in the Mn–O stretching vibrations as detected in Raman spectra. Additionally, the carbon scaffold may influence the crystal growth behavior of MnO$_2$, potentially determining its polymorphic

Open Access Article. Published on 11 May 2026. Downloaded on 6/1/2026 10:54:30 PM.
This article is licensed under a Creative Commons Attribution-NonCommercial 3.0 Unported Licence.

form and associated spectroscopic features. The observed variations in Mn–O vibrational modes further support the existence of direct interfacial interactions, particularly changes in coordination geometry. These interfacial interactions are expected to yield several important consequences: (i) electronic coupling and charge transfer, wherein the conductive carbon matrix enhances electron mobility, crucial for efficient electrochemical performance; (ii) physical confinement and morphological control, where the carbon framework serves as a structural template, directing MnO_2 nucleation and growth while improving crystallinity, surface area, and mechanical stability; and (iii) synergistic effects, where the integrated CB–MnO_2 composite demonstrates superior electrochemical properties, such as higher capacitance, enhanced rate capability, and improved cycling stability, relative to the individual components.[56,57] Fig. 1C, curve d is the Raman spectroscopic response of CB–MnO_2@Zn, showing the emergence of a new vibrational mode at 430 cm^{-1} due to the A_1(TO) or E_1(TO) transverse optical phonon modes of ZnO species[56] Additionally, a noticeable decrease in the intensity ratio of the D and G bands (I_D/I_G) was observed, decreasing from 1.19 for the CB–MnO_2 composite to 1.04 for the Zn^{2+}-intercalated CB–MnO_2@Zn material. This reduction in the I_D/I_G ratio indicates an enhancement in graphitic ordering and a decrease in structural defects within the carbon matrix. The improved ordering is likely due to the intercalation of Zn^{2+} ion, which may facilitate partial restoration of the sp^2-hybridized carbon framework, thereby increasing the structural integrity and electronic conductivity of the composite.

Thermogravimetric analysis (TGA, Fig. 1D) and differential thermal analysis (DTA, SI, Fig. S2) were performed to evaluate the thermal stability of the CB–MnO_2 nanocomposite. The TGA curve shows an initial rapid weight loss up to approximately 160 °C (Case 1), which is primarily attributed to the removal of physiosorbed and chemisorbed water molecules, as well as surface hydroxyl groups. A subsequent slow weight loss observed around 300 °C and 550 °C (Case 2) corresponds to the partial decomposition of the MnO_2 lattice and the carbon framework, along with the loss of lattice oxygen. These processes lead to the formation of lower-valence manganese oxide phases, such as Mn_2O_3 and Mn_3O_4, consistent with literature reports.[58] Overall, these results confirm the successful formation of the CB–MnO_2 nanocomposite and demonstrate its reasonably good thermal stability across a broad temperature range. Interestingly, TGA of the Zn^{2+} intercalated CB–MnO_2 composite (Fig. 1d, curve b) exhibited a distinct two-step thermal decomposition profile, highlighting the increased structural and compositional complexity introduced by Zn^{2+} intercalation. The first major weight loss event was observed around 300 °C, corresponding to the decomposition of surface-bound functional groups and loosely bound oxygen species. A second, more gradual decomposition occurred near 600 °C, likely associated with the breakdown of the manganese oxide framework and carbon matrix. Notably, the overall weight loss in the Zn^{2+} intercalated composite was significantly reduced compared to the non-intercalated counterpart. This reduced mass loss indicates enhanced thermal stability, suggesting that Zn^{2+} intercalation reinforces the composite structure through stronger interfacial interactions and improved bonding between the carbon matrix and MnO_2 network. These findings collectively point to a more thermally robust nanocomposite architecture enabled by Zn^{2+} integration. The TGA data of the individual control samples (CB and MnO_2) are not presented, as their thermal decomposition behaviors are well documented in the literature[59,60] and are not directly relevant to the primary objective of assessing the thermal stability of the composite material.

FESEM was employed to examine the surface morphology of the synthesized materials. FESEM images of the individual components, pristine CB (Fig. 1E) and MnO_2 (Fig. 1F) revealed typical globular, agglomerated nanoscale structures, resembling spherical clusters. In contrast, the CB–MnO_2 (Fig. 1G) nanocomposite displayed a distinct needle-like morphology. This significant morphological transformation is attributed to the chemical interactions between oxygen functional groups of carbon black and MnO_2 in the composition. Energy dispersive X-ray analysis (EDAX) was performed on the CB–MnO_2 nanocomposite (SI, Fig. S3). The EDAX spectrum confirmed the presence of carbon (C; 58.1%), oxygen (O; 22.6%), manganese (Mn; 17.1%), and potassium (K; 1.9%), thereby verifying the successful incorporation of MnO_2 onto the CB matrix. Control EDAX values of CB (C: 92.6%; N; 4.3%; O-2.7%; S: 0.4 impurities) and MnO_2 (Mn; 58.8%; C: 29.6%; K: 11.6%) showed significant variation in the content. The notable reduction in potassium content in the CB–MnO_2 nanocomposite (1.9%), as compared to pure MnO_2 (11.6%), likely arises from a combination of dilution effect, ion exchange or leaching during synthesis and structural reconfiguration at the carbon interface. When MnO_2 is integrated onto the CB surface, the relative abundance of K^+ ions naturally decreases due to the high carbon content of the composite matrix, effectively diluting the potassium. Additionally, since the composite synthesis especially was conducted under aqueous conditions, loosely bound or intercalated K^+ ions within the MnO_2 tunnels may be partially exchanged with H^+ or leached into the medium, leading to a lower residual K^+ content. Moreover, the strong interaction between MnO_2 and the CB surface may induce a partial reorganization of the MnO_2 framework, altering its tunnel or layered structure and reducing the necessity or capacity for K^+ stabilization. Fig. 1H shows the FESEM images of the CB–MnO_2@Zn sample, revealing a distinctive star-shaped, needle-like morphology, indicative of significant structural reorganization upon Zn^{2+} intercalation. This unique morphology was further supported by EDX spectroscopy (Fig. 1H and SI, Fig. S3D), which confirmed the elemental composition as: C – 47.4%, O – 23.9%, Mn – 15.3%, Zn – 9.2%, K – 3.0%, and Cl – 1.1%. Notably, the K^+ content increased from 1.9% in the CB–MnO_2 sample to 3.0% in the Zn-intercalated CB–MnO_2@Zn composite. This increase in K^+ content may plausibly be attributed to a few factors: (i) ion-exchange processes during Zn^{2+} intercalation, where K^+ ions from the electrolyte or precursor solution become incorporated into the MnO_2 structure or adsorbed onto the surface; (ii) the stabilization of tunnel-

© 2026 The Author(s). Published by the Royal Society of Chemistry

Open Access Article. Published on 11 May 2026. Downloaded on 6/1/2026 10:54:30 PM.
This article is licensed under a Creative Commons Attribution-NonCommercial 3.0 Unported Licence.

type or layered α-MnO_2 phases that can host alkali metal ions such as K^+ within their structural cavities; and (iii) the enhanced affinity of the modified surface for K^+ adsorption due to changes in surface charge and coordination environment post Zn^{2+} incorporation. These factors collectively suggest that Zn^{2+} intercalation not only alters the morphology but also affects the ionic composition of the nanocomposite.

To gain deeper molecular-level insights into the chemical states and bonding environments, XPS analysis was conducted on the individual components – carbon black (CB) and α-MnO_2 (SI, Fig. S4) – as well as on the CB–MnO_2 composite, both in the absence and presence of Zn^{2+} ions. For MnO_2, the Mn $2p_{3/2}$ peak was observed at 642.2 eV with additional components at lower binding energies (641 eV) indicating the presence of Mn^{3+} or Mn^{2+} arising from surface defects, sub-oxides, or partial reduction. Pure tetravalent MnO_2 yields predominantly Mn^{4+} signals while mixed valence states appear when non-stoichiometry or surface defects are present.[61–63] The comparatively low CPS intensity observed for the O 1s spectrum in Fig. S4A is attributed to the intrinsically low oxygen content in pure carbon black (CB). In CB, oxygen exists only as minor surface functional groups, such as hydroxyl, carbonyl, or adsorbed oxygen-containing species, rather than as a bulk constituent, resulting in a relatively weak photoelectron signal. Similarly, the reduced C 1s intensity in Fig. S4B arises from the negligible carbon content in pure MnO_2, where carbon is present only as trace adventitious species originating from unavoidable surface contamination during air exposure and sample handling. As the XPS peak intensity is directly proportional to the elemental concentration (and influenced by the photoionization cross-section), the observed lower CPS values are fully consistent with the intrinsic composition of the respective materials. Fig. 2 presents high-resolution XPS spectra of the C 1s, O 1s, Mn $2p_{3/2}$ and Mn $2p_{5/2}$, and Zn $2p_{3/2}$ and Zn $2p_{5/2}$ energy levels for the CB–MnO_2 and CB–MnO_2@Zn composites. A noticeable decrease in the intensity of the C 1s peak in the CB–MnO_2 composite compared to pristine CB indicates significant chemical interactions between carbon atoms and oxygen species originating from MnO_2. This is corroborated by an enhanced O 1s signal, implying the formation of C–O bonds and metal–oxygen linkages at the interface. The presence of functional groups such as –C=O, –COOH, and –C–OH (from graphitic edges or surface oxygen functionalities of CB) further supports the development of a chemically integrated carbon–manganese oxide nanocomposite. The Mn 2p spectra reveal the presence of multiple manganese oxidation states, including Mn^{3+} (as MnOOH) and Mn^{4+} (as MnO_2) along with mixed-valence Mn^{4+}/Mn^{3+} species, typical of stable manganese oxide phases and defective MnO_2 species.[58,64,65] In the Zn-incorporated sample (CB–MnO_2@Zn), XPS revealed Zn $2p_{3/2}$ signals with binding energies at 1022.1 eV and 1023.3 eV, corresponding to zinc hydroxy sulfate (ZHS) and Zn^{2+}/ZnO species, respectively. These assignments are in agreement with the previous literature.[66] Notably, the Mn 2p orbital spin–orbit splitting increases upon Zn^{2+} incorporation, from 11.1 eV in CB–MnO_2 (Mn $2p_{5/2}$ at 642.4 eV and Mn $2p_{3/2}$ at 653.5 eV) to 12.1 eV in CB–MnO_2@Zn (Mn $2p_{5/2}$ at 642.2 eV and Mn $2p_{3/2}$ at 654.3 eV). This shift suggests a modified electronic structure and a higher average valence state in the Zn-doped system.[67] Furthermore, the marked increment in the oxygen-vacancies was found at 532.1 eV for the O 1s level due to the defective MnO_2 structures. Interestingly, while the Mn valence increases locally, the average Mn oxidation state slightly decreases due to Zn^{2+} substitution, which is known to disrupt the MnO_2 lattice and introduce abundant oxygen vacancies. These vacancies may facilitate enhanced Zn^{2+} intercalation, underlining the

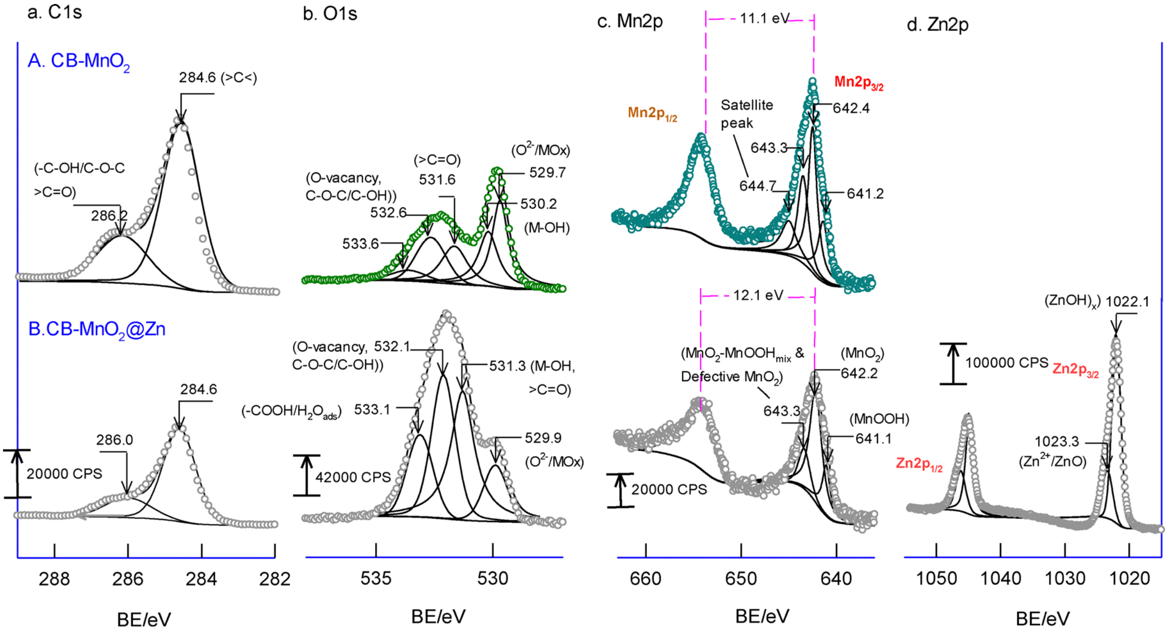

Fig. 2 XPS analysis of (A) CB–MnO_2 and (B) CB–MnO_2@Zn for the elements C 1s, O 1s, Mn 2p and Zn 2p.

© 2026 The Author(s). Published by the Royal Society of Chemistry

Open Access Article. Published on 11 May 2026. Downloaded on 6/1/2026 10:54:30 PM.
This article is licensed under a Creative Commons Attribution-NonCommercial 3.0 Unported Licence.

promising potential of CB–MnO_2@Zn for aqueous zinc-ion hybrid electrochemical applications.

The N_2 adsorption–desorption isotherms of all samples (Fig. 3A–D) exhibit typical type-IV behavior with a clear hysteresis loop, confirming their mesoporous nature. As shown in Fig. 3A, pristine CB displays a low specific surface area of 24.08 m^2 g^{-1} with a large average pore size of 44.52 nm, indicating limited active surface availability. In Fig. 3B, MnO_2 shows a significantly higher surface area of 130.50 m^2 g^{-1} and a reduced pore size of 20.53 nm, reflecting its nanostructured mesoporous framework. However, excessive surface area in pure MnO_2 may lead to structural instability and aggregation. The CB–MnO_2 composite (Fig. 3C) exhibits a moderate surface area of 67.58 m^2 g^{-1} and an average pore size of 19.88 nm, suggesting uniform MnO_2 anchoring on the CB matrix. This composite structure improves conductive pathways while preserving sufficient mesoporosity for the ions diffusion. Notably, the optimized CB–MnO_2@Zn sample (Fig. 3D) presents a surface area of 70.95 m^2 g^{-1} with a smaller pore size of 12.65 nm. The reduced pore diameter indicates a more compact and uniform mesoporous structure after Zn incorporation. Such balanced surface area and optimized mesopores facilitate rapid electrolyte penetration and efficient charge transfer. Therefore, the superior electrochemical performance of CB–MnO_2@Zn can be attributed to its synergistically tuned porous architecture and enhanced structural stability.

3.2. CB–MnO_2@Zn as a supercapacitor

Fig. 4A (curves a and b) presents the CV responses of the GP/CB–MnO_2 electrode in the presence and absence of 1 mM $ZnSO_4$, dissolved in 0.1 M KCl as the supporting electrolyte. In the absence of Zn^{2+} ions, a purely capacitive CV profile was observed, indicating non-faradaic behavior. However, upon the introduction of Zn^{2+} ion, a distinct faradaic peak emerged at an apparent standard electrode potential (E°) of approximately 0.5 V *vs.* Ag/AgCl, suggesting selective redox activation. This response is

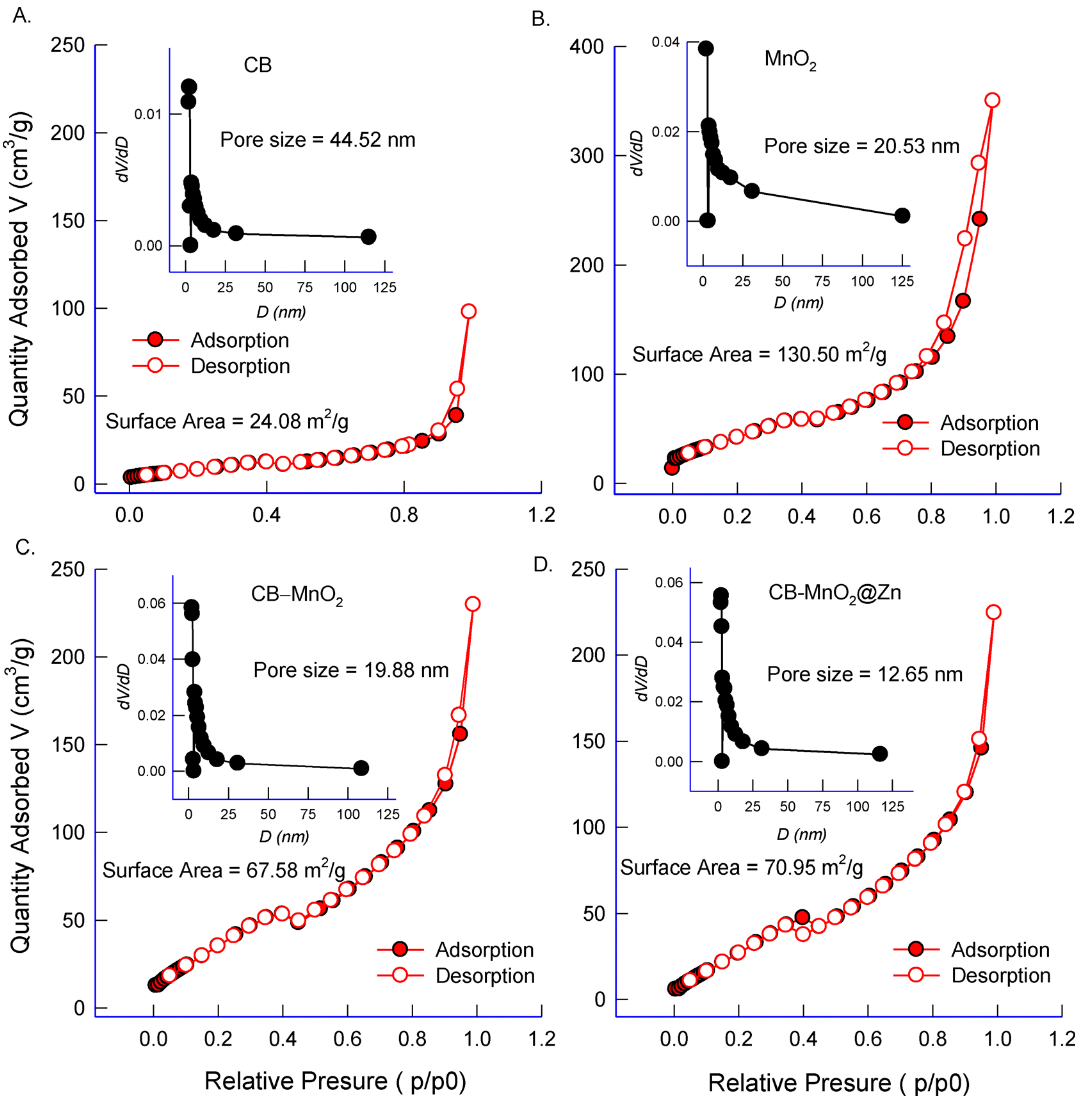

Fig. 3 BET analysis of (A) CB, (B)MnO_2, (C) CB–MnO_2 and (D) CB–MnO_2@Zn.

© 2026 The Author(s). Published by the Royal Society of Chemistry

Open Access Article. Published on 11 May 2026. Downloaded on 6/1/2026 10:54:30 PM.
This article is licensed under a Creative Commons Attribution-NonCommercial 3.0 Unported Licence.

attributed to Zn^{2+}-mediated facilitation of Mn redox processes, enhancement of electrical conductivity, and possible structural modifications not accessible in the pristine CB–MnO_2 system. Zn^{2+} ion appear to serve dual roles: promoting electrochemical activity and contributing to structural reorganization. To optimize the Zn^{2+} concentration, a series of CV experiments were conducted using varying concentrations of $ZnSO_4$ (0.5 mM, 1 mM, 5 mM, and 10 mM) in 0.1 M KCl (SI, Fig. S6). Among these, 1 mM $ZnSO_4$ yielded the highest CV current response and specific capacitance, indicating it as the optimal electrolyte composition for further investigations. At this concentration, Zn^{2+} ions are likely present in sufficient quantity to intercalate into the MnO_2 lattice and facilitate reversible Mn^{4+}/Mn^{3+} redox transitions, without reaching levels that could lead to oversaturation, reduced ion mobility, or the formation of insoluble species such as $Zn(OH)_2$ or basic zinc salts. In contrast, lower concentrations (*e.g.*, 0.5 mM) may provide insufficient Zn^{2+} to fully engage redox-active sites, while higher concentrations (5 mM and 10 mM) could induce double-layer crowding, lower ionic conductivity, or trigger side reactions such as Zn^{2+} hydrolysis and surface passivation, all of which detract from electrochemical performance. Therefore, 1 mM $ZnSO_4$ offers an optimal balance of redox activity, ionic transport, and structural stability and is thus selected as the standard condition for preparing the GP/CB–MnO_2@Zn composite used in this study.

Furthermore, the influence of scan rate on the electrochemical behavior of the GP/CB–MnO_2 nanocomposite was investigated by recording CV curves at scan rates ranging from 5 to 100 mV s^{-1}, both in the absence (Fig. 4B) and presence (Fig. 4C) of Zn^{2+} ions. In both scenarios, the peak current increased with increasing scan rate, indicating a diffusion-controlled charge transport process and efficient electron transfer kinetics at the electrode–electrolyte interface. Notably, in the presence of Zn^{2+} ions, the redox peaks became more pronounced, suggesting an enhanced faradaic contribution. To quantitatively distinguish the charge storage contributions, Dunn's method was employed to separate the capacitive-controlled and diffusion-controlled processes at different scan rates. According to the

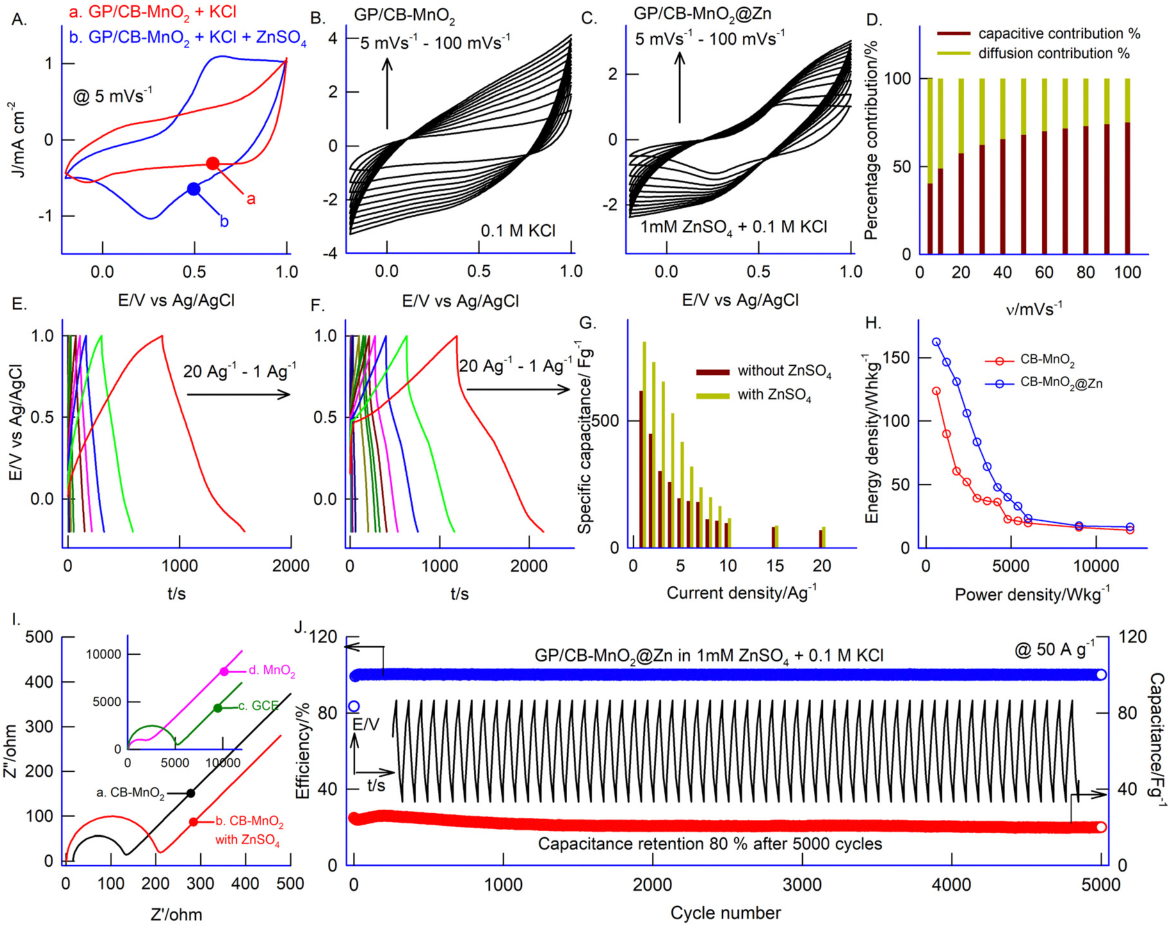

Fig. 4 (A) Comparative CV response of (a) GP/CB–MnO_2 and (b) GP/CB–MnO_2@Zn at a scan rate of 5 mV s^{-1}. Effect of scan rates from 5 to 100 mV s^{-1} on (B) GP/CB–MnO_2 in 0.1 M KCl and (C) GP/CB–MnO_2@Zn in 0.1 M KCl + 1 mM $ZnSO_4$. (D) Bar graph showing the capacitive contribution calculated using Dunn's method. Galvanostatic charge–discharge measurements of (E) GP/CB–MnO_2 and (F) GP/CB–MnO_2@Zn at a range of current densities from 20 Ag^{-1} to 1 Ag^{-1}. (G) Comparative bar graph of the specific capacitances of GP/CB–MnO_2 and GP/CB–MnO_2@Zn. (H) Comparative graph of energy density *vs.* power density for GP/CB–MnO_2 and GP/CB–MnO_2@Zn. (I) EIS analysis of different modified and unmodified electrodes in 5 mM $[Fe(CN)_6]^{3-}$ containing 0.1 M KCl at an applied potential of 0.2 V *vs.* Ag/AgCl. (J) Galvanostatic charge–discharge measurement of GP/CB–MnO_2@Zn for continuous 5000 cycles in 1 mM $ZnSO_4$ + 0.1 M KCl at 50 Ag^{-1} input current.

© 2026 The Author(s). Published by the Royal Society of Chemistry

Open Access Article. Published on 11 May 2026. Downloaded on 6/1/2026 10:54:30 PM.
This article is licensed under a Creative Commons Attribution-NonCommercial 3.0 Unported Licence.

power-law relationship ($i = av^b$), the b-values were determined from the slope of $\log(i)$ *versus* $\log(v)$ plots (SI, Fig. S7), providing insight into the dominant charge storage mechanism.[68] Furthermore, the current response at a fixed potential was expressed as

$$i(V) = k_1 v + k_2 v^{1/2} \tag{1}$$

where $k_1 v$ and $k_2 v^{1/2}$ correspond to the capacitive and diffusion-controlled contributions, respectively. The fitting results derived from the linear plots of $i(V)/v^{1/2}$ *versus* $v^{1/2}$ enabled the quantitative estimation of each contribution at various scan rates (SI, Fig. S8). The resulting capacitive contribution graph clearly demonstrates an increasing capacitive-dominated behavior with increasing scan rate (Fig. 4D), indicating improved surface-controlled kinetics and rapid charge transfer characteristics of the composite electrode. These findings confirm that the synergistic interaction between MnO_2 and conductive carbon effectively enhances pseudocapacitive behavior, contributing to the superior electrochemical performance.

To further assess the charge-storage performance, galvanostatic charge–discharge (GCD) measurements were carried out across a wide range of current densities (1–20 Ag^{-1}) under Zn^{2+}-free (Fig. 4E) and Zn^{2+}-containing (Fig. 4F) electrolyte conditions. The introduction of Zn^{2+} ions significantly improved the charge–discharge behavior, highlighting the synergistic role of Zn^{2+} intercalation in boosting the overall electrochemical activity of the nanocomposite. Interestingly, in the Zn^{2+}-containing system, a sharp voltage increase was observed within the initial seconds of the charging process. This behavior is consistent with the findings reported by Wu *et al.*[27] for pristine α-MnO_2 and is plausibly attributed to the initial energy barrier associated with Zn^{2+} ion intercalation into the MnO_2 framework, coupled with electrode polarization and nucleation effects. Such features are characteristic of redox-active electrode materials undergoing ion insertion, further confirming the pseudocapacitive nature of the system.

Similar to the CV experiments, the effect of Zn^{2+} concentration was also studied in the GCD measurements by measuring the respective capacitance value using the following equation:[16–18]

$$C_{sp} = \frac{i \times \Delta t}{m \times \Delta V} \tag{2}$$

where C_{sp} = specific capacitance, i = input current, Δt = discharge time, m = mass of the electrode and ΔV = potential window. A maximum specific capacitance of 811.6 F g^{-1} and 618.3 F g^{-1} was achieved for the CB–MnO_2 nanocomposite in the presence and absence of Zn^{2+} ions, respectively (Fig. 4G). These values are significantly higher than those reported for most nanocarbon/MnO_2 composite systems in the literature (SI, Table S2). For comparison, a g-C_3N_4/MnO_2 electrode tested in 2 M KOH (0–0.5 V window) delivered a specific capacitance of 148.66 F g^{-1} at 0.5 A g^{-1}, but retained only 50% of its capacitance after 3000 cycles, indicating limited cycling stability.[69] A nanostructured manganese oxide composite showed a capacitance of 182 F g^{-1} at 1 A g^{-1} in 1 M Na_2SO_4 over a 0–1.2 V window. Although it benefited from the extended voltage range and stable electrolyte, low ionic conductivity and absence of cycling data raise concerns about its rate performance and long-term stability.[70] Mesoporous α-MnO_2 synthesized *via* hydrothermal methods exhibited a specific capacitance of 324 F g^{-1} at 0.5 A g^{-1} in 1 M Na_2SO_4 (0–1 V window). Its good performance is attributed to the tunnel-like crystalline structure that facilitates ion intercalation and redox activity, along with reasonable cycling stability.[71] A MnO_2/biochar composite tested in 1 M Na_2SO_4 (0–1 V window) delivered 205.5 F g^{-1} at 0.5 A g^{-1}. The porous, conductive biochar structure supports ion transport and contributes to good initial cycling retention (96.1% after 1000 cycles). However, the capacitance remains moderate, and the limited cycle life data suggest that long-term performance needs further evaluation.[72] A comparative summary of such materials and their supercapacitor performance is provided in SI, Table S2. The substantial enhancement in capacitance upon Zn^{2+} incorporation can be ascribed to the unique pseudo redox activity of the composite and the efficient intercalation/deintercalation of Zn^{2+} ions within the MnO_2 framework. This process contributes to additional redox reactions and facilitates improved ion transport kinetics, thereby enhancing the overall electrochemical performance.

Furthermore, the energy density (E, in Wh kg^{-1}) and power density (P, in W kg^{-1}) of the electrode were calculated using the following equations:[16–18,68]

$$E = \frac{C \times \Delta V^2}{2 \times 3.6} \tag{3}$$

$$P = \frac{E \times 3600}{\Delta t} \tag{4}$$

where E = energy density and P = power density. A maximum energy density of 162.3 Wh kg^{-1} was achieved at a corresponding power density of 600 W kg^{-1} for the CB–MnO_2@Zn electrode, as shown in Fig. 4H. These values of specific capacitance, energy density, and power density are significantly higher than those reported for most MnO_2-based supercapacitor electrodes in the literature (SI, Table S2), highlighting the superior electrochemical performance of the synthesized nanocomposite.

To support the electrochemical findings, electrochemical impedance spectroscopy (EIS) was performed in the presence of a 1 mM $Fe(CN)_6{}^{3-/4-}$ redox couple (Fig. 4I). The bare glassy carbon electrode (GCE) showed the highest charge transfer resistance (R_{CT}) of 2182 Ω, while pristine MnO_2 had an even higher R_{CT} of 5539 Ω, indicating very poor charge transfer. In contrast, the CB–MnO_2 composite had a much lower R_{CT} of 78.9 Ω, showing that the conductive carbon black greatly improved electron transport. When Zn^{2+} was added to the CB–MnO_2 system, the R_{CT} slightly increased to 124.6 Ω, possibly due to partial blockage of active sites or added resistance from Zn^{2+} intercalation for the outer sphere electron-transfer reaction. To test the long-term stability of the cathode, the GP/CB–MnO_2@Zn electrode was subjected to 5000 charge–discharge cycles at a high current density of 50 A g^{-1} (Fig. 4J).

© 2026 The Author(s). Published by the Royal Society of Chemistry

Open Access Article. Published on 11 May 2026. Downloaded on 6/1/2026 10:54:30 PM.
This article is licensed under a Creative Commons Attribution-NonCommercial 3.0 Unported Licence.

Impressively, it maintained a coulombic efficiency of 99% and retained 80% of its original capacitance, demonstrating excellent durability and structural stability under demanding conditions. Such extendable stability is rarely reported in the literature (SI, Table S2).

3.3. *Operando* EQCM and SECM analyses

To gain deeper insights into the Zn^{2+} intercalation mechanism in the CB–MnO_2@Zn composite, *operando* EQCM analysis was performed using a gold (Au) working electrode in an electrolyte containing 1 mM $ZnSO_4$ and 0.1 M KCl. Fig. 5A–C present the representative CV and corresponding EQCM responses of the Au–EQCM/CB–MnO_2 system in this electrolyte. The CV profile exhibited redox features qualitatively similar to those observed for the GP/CB–MnO_2 electrode shown in Fig. 4A. During continuous potential cycling, a progressive increase in mass was detected, indicating the uptake of electroactive species. Using the relationship $M_w = (\Delta m/\Delta Q) \times F$, where Δm is the mass change, ΔQ is the charge, and F is the Faraday constant, the molecular weights (M_w) of the species involved in the interfacial reactions were estimated. Fig. 5C (2nd cycle) highlights the sequential appearance of various molecular weight values corresponding to active species such as $Zn_3(OH)_6SO_4{\cdot}2H_2O$ (414.5 g mol^{-1}), $Zn(OH)_2$ (99.3 g mol^{-1}), $MnO_2{\cdot}0.5H_2O$ (176.6 g mol^{-1}), $Zn_4(OH)_6SO_4{\cdot}2H_2O$ (495.4 g mol^{-1}), ZnO (79.5 g mol^{-1}), and K^+ (40.9 g mol^{-1}) during the forward scan. In the reverse scan, species like $2Zn(OH)_2$ (183.9 g mol^{-1}) and MnO_2 (87.6 g mol^{-1}) were identified. These observations confirm the formation of layered zinc hydroxysulfate (ZHS) intermediates, followed by ZnO and $Zn(OH)_2$ deposition, as well as the intercalation of K^+ ions into the electrode matrix. As a control, EQCM analysis of the CB–MnO_2 composite in the absence of Zn^{2+} revealed the dissolution of the MnO_2 framework, evidenced by the release of Mn^{2+} and Mn^{4+} species (SI, Fig. S9A–C). Additionally, EQCM measurements conducted on a bare Au electrode in the presence and absence of $ZnSO_4$ (with 0.1 M KCl) showed negligible mass changes (in the nanogram range), attributed to minor K^+ interactions with the native gold oxide layer (SI, Fig. S10A–F). Collectively, these results demonstrate the electrochemical stability of the CB–MnO_2@Zn composite and confirm reversible Zn^{2+} intercalation/deintercalation, primarily through the formation of ZHS and ZnO/$Zn(OH)_2$ species, in agreement with previously reported findings.[73–75]

To further support the operando EQCM analysis, a carefully designed *in situ* SECM study was carried out using a GCE/CB–MnO_2 substrate operating at open circuit potential (E_{OCP}), with a Pt ultramicroelectrode (UME) tip biased at −0.25 V *vs.* Ag/AgCl. The experiments were performed in both the absence and presence of 1 mM Zn^{2+} in 0.1 M KCl electrolyte. Prior to SECM

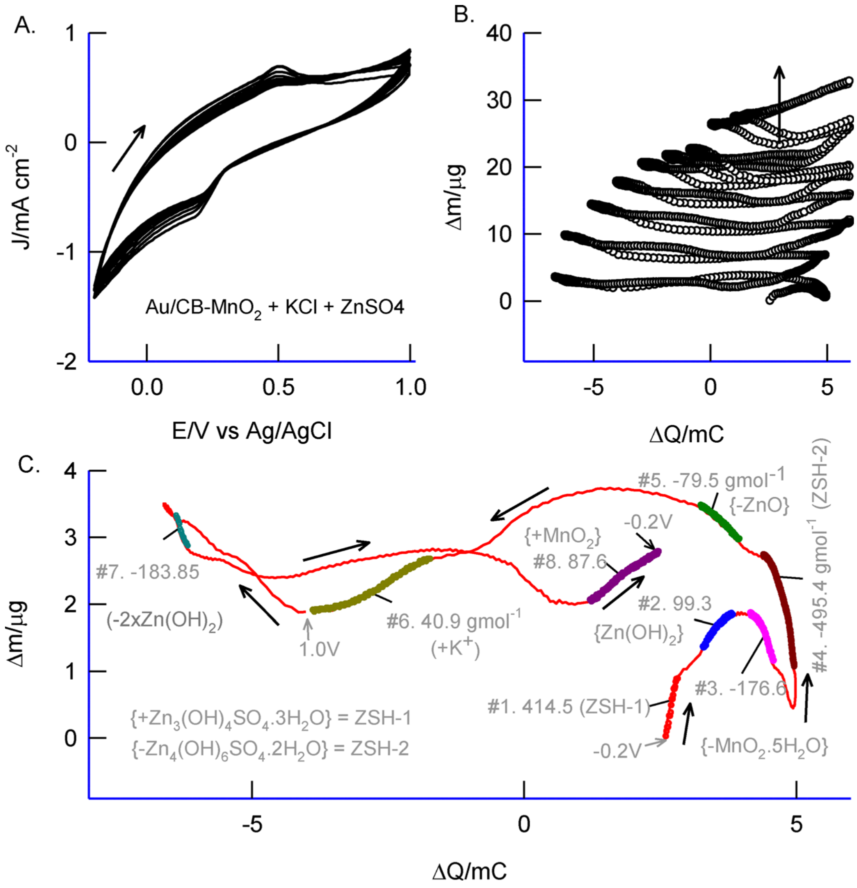

Fig. 5 EQCM responses of Au/CB–MnO_2 with (A)–(C) $ZnSO_4$ containing 0.1 M KCl.

Open Access Article. Published on 11 May 2026. Downloaded on 6/1/2026 10:54:30 PM.
This article is licensed under a Creative Commons Attribution-NonCommercial 3.0 Unported Licence.

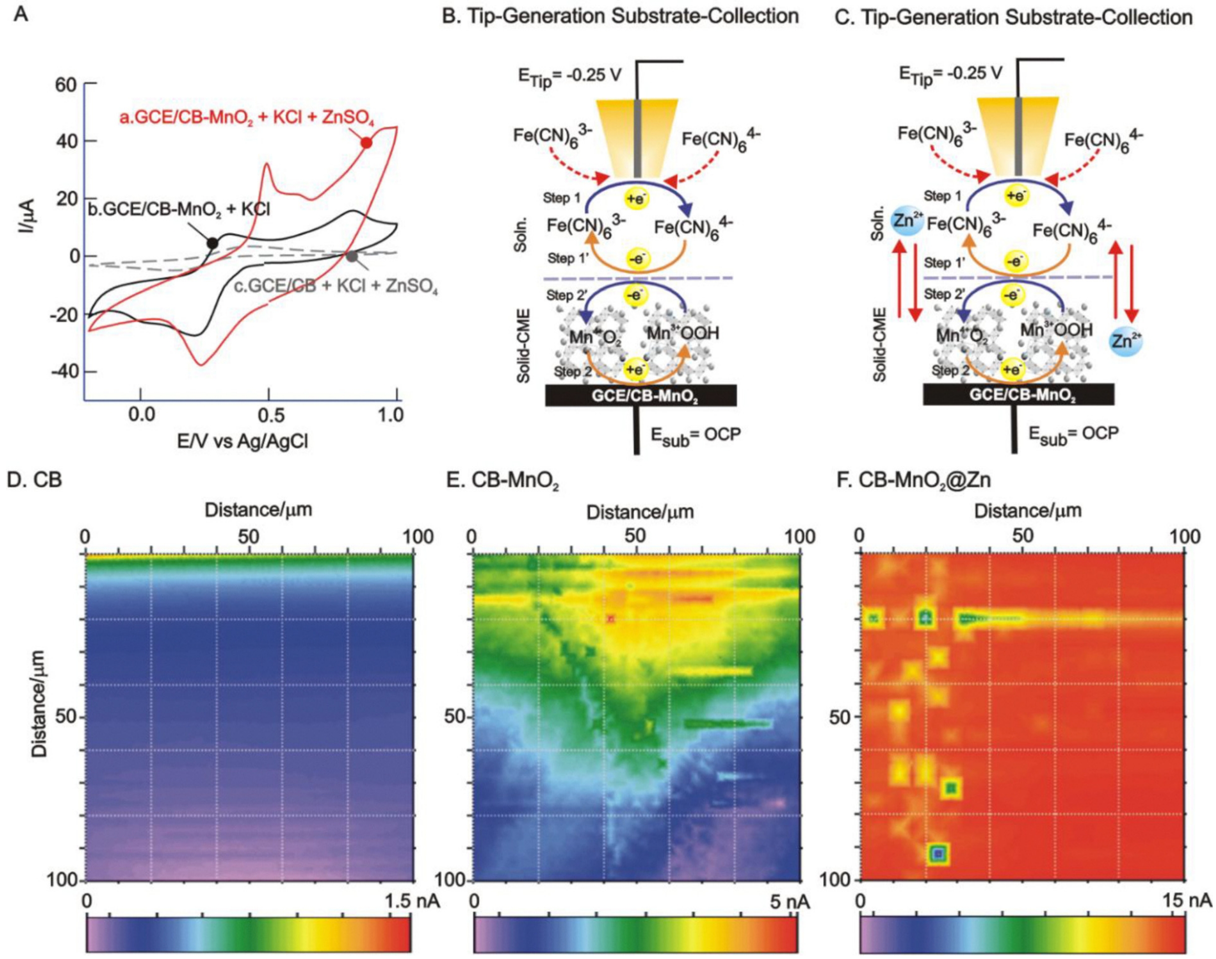

Fig. 6 SECM analysis: (A) CV responses of GCE/CB–MnO$_2$ with (curve a) and without (curve b) ZnSO$_4$ containing KCl and (curve c) shows GCE/CB response in ZnSO$_4$ containing KCl. (B) and (C) Schematic representation of tip-generation substrate–collection mechanisms of the SECM analysis of CB–MnO$_2$ and CB–MnO$_2$@Zn and their respective SECM images (D)–(F).

imaging, CV measurements were conducted using GCE/CB–MnO$_2$ in the presence of $[Fe(CN)_6]^{3-}$ (as a redox mediator) dissolved in 0.1 M KCl, both without and with Zn^{2+} (Fig. 6A). In the absence of Zn^{2+}, a well-defined redox couple corresponding to the $Fe^{III/II}(CN)_6^{3-/4-}$ redox reaction was observed with a formal potential (E°) around 0.25 V *vs.* Ag/AgCl. Interestingly, in the presence of Zn^{2+}, the redox peaks became approximately twice as intense, along with a positive shift in E° to ∼0.4 V *vs.* Ag/AgCl (Fig. 6A). This behavior suggests a strong interaction between Zn-intercalated CB–MnO$_2$ (CB–MnO$_2$@Zn) and the redox couple, likely mediated by Zn-assisted MnO$_2$/MnOOH redox transitions that enhance the electron transfer kinetics of the $Fe(CN)_6^{3-/4-}$ couple. This significant modulation of current response in the presence of Zn^{2+} was exploited for SECM imaging. The imaging protocol was designed based on a two-step redox mediation mechanism: (Step 1) $Fe(CN)_6^{3-}$ is electrochemically reduced at the Pt UME to $Fe(CN)_6^{4-}$, which then (Step 2) transfers an electron to $Mn^{4+}O_2$ on the substrate surface, reducing it to $Mn^{3+}OOH$. The reverse electron transfer (Step 1′) reoxidizes $Fe(CN)_6^{4-}$ to $Fe(CN)_6^{3-}$. Subsequently, $Mn^{3+}OOH$ is reoxidized to MnO$_2$ *via* Zn^{2+}-intercalation under open circuit conditions (Step 2′). Fig. 6B and C schematically illustrate these reaction pathways and experimental conditions. The SECM images of CB–MnO$_2$ and CB–MnO$_2$@Zn are shown in Fig. 6E and F, respectively. In the absence of Zn^{2+}, a diffuse, cloud-like distribution of surface activity was observed. In contrast, with Zn^{2+} present, distinct, crystallite-like active spots emerged, along with a twofold increase in the probe current. As a control, GCE/CB was also tested under identical conditions (Fig. 6D and SI, Fig. S12), revealing a blurred image with minimal probe current response. These results collectively confirm the enhanced redox activity of the CB–MnO$_2$@Zn system, facilitated by Zn^{2+} intercalation, and demonstrate its effective electrochemical performance.

3.4. CB–MnO$_2$@Zn as a cathode for a Zn^{2+}/K$^+$ ion hybrid battery

The as-synthesized GP/CB–MnO$_2$@Zn composite was further employed as the cathode, paired with a Zn metal anode, using an electrolyte consisting of 1 mM ZnSO$_4$ and 0.1 M KCl. Initially, CV studies were conducted in a two-electrode

© 2026 The Author(s). Published by the Royal Society of Chemistry

Open Access Article. Published on 11 May 2026. Downloaded on 6/1/2026 10:54:30 PM.
This article is licensed under a Creative Commons Attribution-NonCommercial 3.0 Unported Licence.

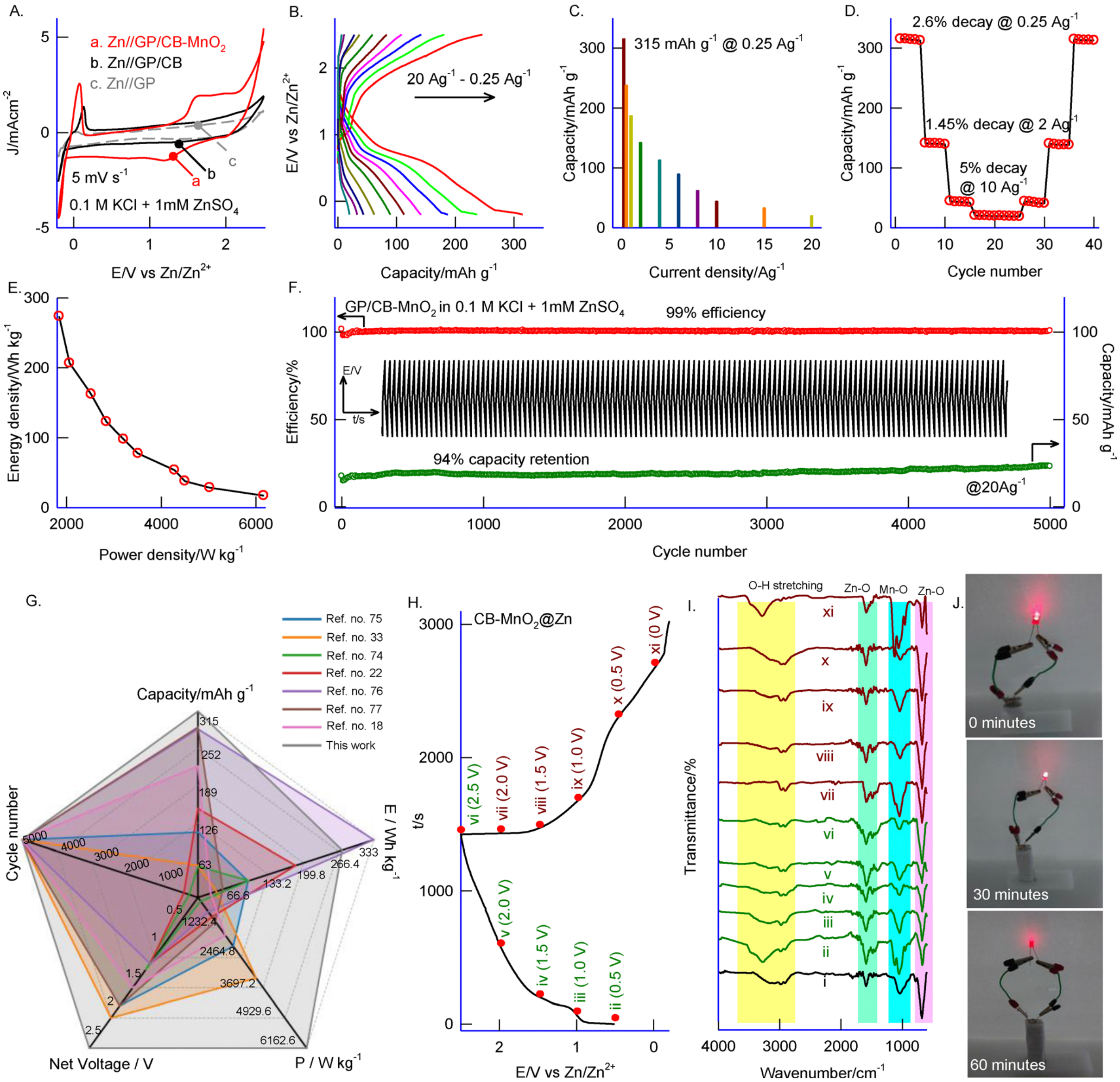

Fig. 7 (A) CV responses of (curve a), Zn‖GP/CB–MnO_2, (curve b) Zn‖GP/CB and (curve c) Zn‖GP cells in an extended potential window (−0.2 to 2.5 V *vs.* Zn/Zn^{2+}) in 1 mM $ZnSO_4$ containing 0.1 M KCl at a scan rate of 5 mV s^{-1}. (B) Potential *vs.* capacity graph of Zn‖GP/CB–MnO_2@Zn in 1 mM $ZnSO_4$ containing 0.1 M KCl at a range of current densities from 20 Ag^{-1} to 0.25 Ag^{-1}. (C) Derivative bar graph of the capacities obtained *vs.* respective current densities. (D) Rate performance profile of Zn‖GP/CB–MnO_2@Zn. (E) Energy density *vs.* power density of Zn‖GP/CB–MnO_2@Zn. (F) Capacity retention and efficiency *vs.* cycle number profiling of Zn‖GP/CB–MnO_2@Zn (inset: 1000 cycles of GCD curves obtained). (G)–(H) *Ex situ* FT-IR spectra measured at different potentials during charging and discharging processes. (i) Lighting of an LED using two series connection of a Zn‖GP/CB–MnO_2@Zn micro-pouch cell battery at 0 minutes, 30 minutes and 60 minutes.

configuration, connecting the GP/CB–MnO_2@Zn cathode with the Zn anode in the same electrolyte. As shown in Fig. 7A, the measurements were performed over a wide potential window ranging from −0.2 V to 2.5 V *vs.* Zn/Zn^{2+}. Notably, a highly reversible Zn redox peak was observed around 0 V *vs.* Ag/AgCl, corresponding to the stripping and deposition of Zn^{2+}/Zn, which indicates well-defined Zn plating/stripping behavior. Additionally, Mn redox activity was evident within the 1.8–2.2 V range *vs.* Zn/Zn^{2+}, occurring efficiently even at a high potential of 2.5 V under these conditions. To the best of our knowledge, such highly reversible Zn/Zn^{2+} redox activity in this potential range has not been reported previously for aqueous Zn-ion battery systems (SI Table S3). Importantly, no significant side reactions such as the oxygen evolution reaction (OER) or the hydrogen evolution reaction (HER) were observed, indicating excellent electrochemical stability. For instance, in 2024, a MnO_2/Mn_2O_3–GO/CNF composite electrode, evaluated in 6 M KOH within a 0–1.5 V potential window, exhibited moderate specific capacity and cycling stability, though its performance was inherently limited by the narrow aqueous voltage range.[76] A mesoporous MC–MnO_2 electrode, synthesized *via* hydrothermal and co-precipitation methods, was tested in 2 M $ZnSO_4$ + 0.1 M

Open Access Article. Published on 11 May 2026. Downloaded on 6/1/2026 10:54:30 PM.
This article is licensed under a Creative Commons Attribution-NonCommercial 3.0 Unported Licence.

$MnSO_4$ electrolyte over a 0.6–1.9 V window. It demonstrated efficient Zn^{2+} intercalation and delivered a specific capacity of 227 mAh g^{-1} at 0.2 A g^{-1}, yet its net operating voltage (~1.3 V) and capacity fading over prolonged cycling constrained its long-term performance.[77] Similarly, a PANI–MnO_2/CC (polyaniline–MnO_2 on carbon cloth) composite, fabricated *via* electrodeposition and operated in 2 M $ZnSO_4$ + 0.2 M $MnSO_4$ between 0.8 and 1.9 V, achieved a high capacity of 285 mAh g^{-1} and an energy density of 333.3 Wh kg^{-1}. However, its low capacity retention (61.7% after 800 cycles) and limited rate capability restricted its viability for durable applications.[78] Meanwhile, a Gr–MnO_2 (graphene–MnO_2) composite electrode, produced through laser modification and tested in 2 M $ZnSO_4$ + 0.1 M $MnSO_4$ over a 1.0–2.0 V range, delivered a capacity of 233 mAh g^{-1} at 1 A g^{-1}. Despite the conductive benefits of graphene, the system showed only 71% retention after 1000 cycles and poor capacitance retention, attributed to insufficient structural stability and a limited effective operating voltage (~1 V).[79]

To optimize the electrolyte concentration, electrochemical measurements were performed using varying concentrations of $ZnSO_4$ (SI, Fig. S13). Among these, the 1 mM $ZnSO_4$ solution consistently delivered the highest electrochemical performance, as evidenced by both cyclic voltammetry (CV) and galvanostatic charge–discharge (GCD) analyses. This superior performance at 1 mM is attributed to the optimal intercalation of Zn^{2+} ions into the MnO_2 lattice without inducing site saturation or structural hindrance. Additionally, this concentration offered a favorable balance between ionic conductivity and Zn^{2+} ion diffusion, thereby facilitating efficient redox kinetics and enhanced capacitive behavior.

Furthermore, the Zn‖GP/CB–MnO_2@Zn cell was evaluated across a wide range of current densities from 0.25 A g^{-1} to 20 A g^{-1} (Fig. 7B). Based on the derivative plots, the highest specific capacity of 315 mAh g^{-1} was achieved at 0.25 A g^{-1} (Fig. 7C), calculated using the equation:[76–79]

$$C = \frac{I\Delta t}{m} \tag{5}$$

The rate capability of the device (Fig. 7D) demonstrated minimal capacity degradation, with only a 5% decrease even at a high current density of 10 A g^{-1}. Furthermore, the device delivered an impressive energy density of 273.4 Wh kg^{-1} at a power density of 1844.4 W kg^{-1} (Fig. 7E), underscoring its outstanding energy storage characteristics. Comparative performance data with other reported Zn-ion batteries are summarized in SI Table S3. For long-term cycling stability, the device was subjected to 5000 continuous charge/discharge cycles, retaining 94% of its initial capacity and delivering 99% coulombic efficiency (Fig. 7F), thereby confirming its excellent durability and reliability for practical applications. The hybrid supercapacitor–battery performance of the present system, specifically its capacity, energy density, power density, operating voltage, and cycle life, surpasses that of numerous previously reported devices. A comparative radar plot is provided in Fig. 7G, with detailed data summarized in SI, Table S3.[18,22,80–85] To further investigate the Zn^{2+} intercalation mechanism within the nanocomposite, *ex situ* FTIR analyses were carried out at different states of charge and discharge (Fig. 7H). The spectra revealed significant variations in characteristic vibrational bands: –OH stretching at 3295 cm^{-1}, Zn–O vibrations at 1595 and 690 cm^{-1}, and Mn–O stretching at 1064 cm^{-1} (Fig. 7I). During charging at 2.5 V, a reduction in –OH and Mn–O stretching band intensities was observed, indicating Zn^{2+} intercalation into the MnO_2 matrix. Upon discharge, the –OH band returned to its original intensity, while the Mn–O band exhibited structural distortion, confirming Zn^{2+} deintercalation. To demonstrate the practical applicability of the device, a red LED was successfully powered using the as-fabricated micro-pouch cell, which remained illuminated for extended durations (Fig. 7J). Overall, the newly developed CB–MnO_2@Zn composite cathode demonstrated efficient Zn^{2+} ion intercalation, leading to enhanced performance in both supercapacitor and Zn^{2+}/K^{+} hybrid ions battery applications.

3.5. Post cycle stability analysis of CB–MnO_2@Zn

The post-cycling structural stability of the CB–MnO_2@Zn cathode was evaluated using FT-IR (Fig. 8A) and Raman spectroscopy (Fig. 8B) after prolonged galvanostatic charge–discharge cycling (1000, 2000, and 5000 cycles). As shown in Fig. 8A, the pristine electrode exhibits characteristic O–H stretching vibrations around ~3400 cm^{-1}, indicating adsorbed water or surface hydroxyl groups. The distinct bands corresponding to Zn–O and Mn–O stretching vibrations observed in the 400–800 cm^{-1} region confirm the formation of Zn-modified MnO_2. After 1000, 2000, and 5000 cycles, these characteristic vibrational peaks remain clearly visible without significant peak shifting or disappearance, indicating the preservation of the metal–oxygen framework. Only slight variations in intensity are observed, which may be attributed to minor surface reconstruction or electrolyte interaction during repeated cycling. Importantly, the retention of Mn–O and Zn–O vibrational modes confirms the structural robustness of the composite cathode. The Raman spectra in Fig. 8B further validate the structural integrity of the material. The prominent Mn–O lattice vibration peak (around ~600–650 cm^{-1}) remains stable after extended cycling, suggesting that the MnO_2 framework does not undergo significant phase transformation. The presence of D and G bands (~1350 and ~1580 cm^{-1}) corresponds to the carbon black matrix. The calculated I_D/I_G ratio changes slightly from 1.04 (pristine) to 0.83 (1000 cycles), 0.87 (2000 cycles), and 1.10 (5000 cycles). These marginal variations indicate minor defect rearrangement in the carbon network but no severe structural degradation. Overall, the combined FT-IR and Raman results demonstrate that the CB–MnO_2@Zn cathode maintains its chemical bonding environment and carbon framework even after 5000 charge–discharge cycles. The preserved Mn–O and Zn–O structures, along with stable D/G band characteristics, confirm the excellent structural durability and strong interfacial interaction within the composite. This structural stability directly supports the superior long-term electrochemical cycling performance of the optimized CB–MnO_2@Zn cathode.

© 2026 The Author(s). Published by the Royal Society of Chemistry

Open Access Article. Published on 11 May 2026. Downloaded on 6/1/2026 10:54:30 PM.
This article is licensed under a Creative Commons Attribution-NonCommercial 3.0 Unported Licence.

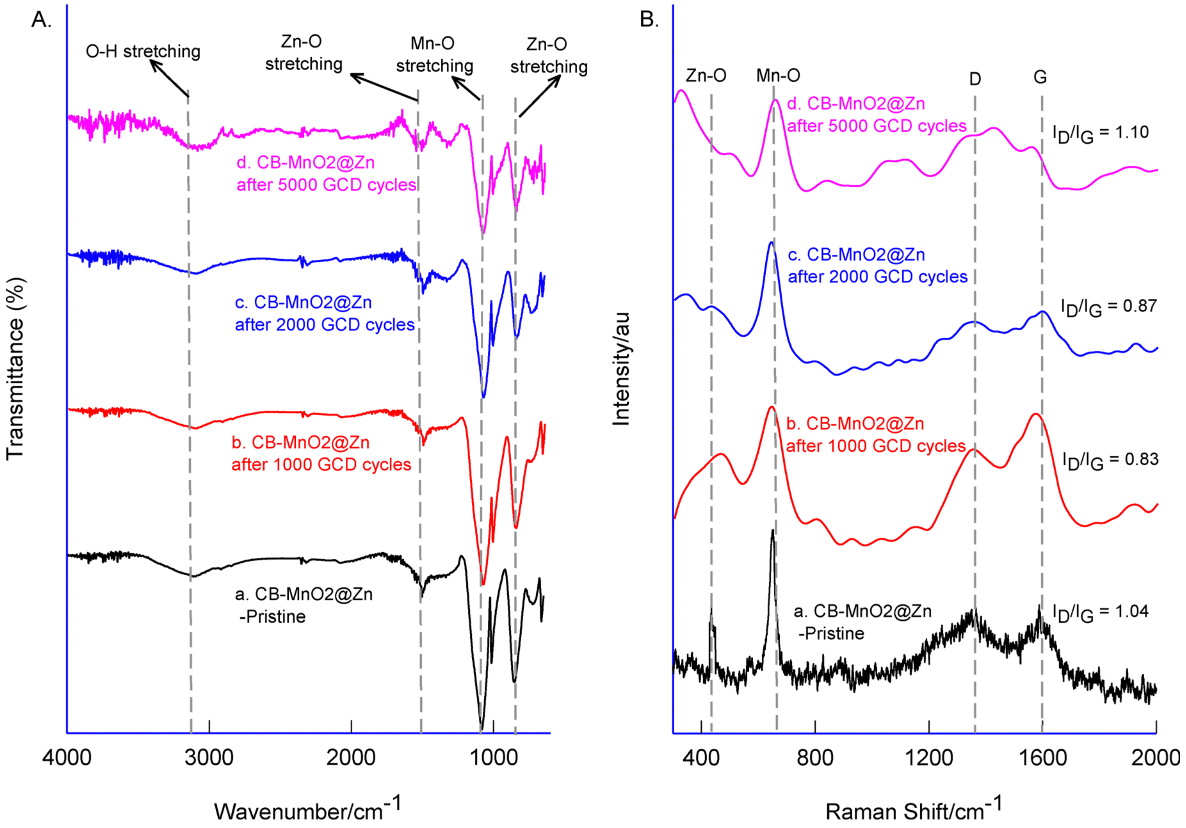

Fig. 8 Post-cycling stability analysis of the CB–MnO_2@Zn cathode: (A) FT-IR spectra and (B) Raman spectra.

4. Conclusions

A Zn^{2+}-intercalated carbon black–MnO_2 composite, denoted as CB–MnO_2@Zn, was synthesized through a two-step process involving chemical conditioning followed by electrochemical treatment. Physicochemical characterization using XRD, FTIR, Raman spectroscopy, TGA, and XPS revealed that the incorporation of conductive carbon material significantly enhanced the otherwise poor electronic conductivity of α-MnO_2 by serving as a conductive scaffold. This structural integration facilitated efficient electron transport and promoted Zn^{2+} intercalation. Post intercalation, the initially poorly crystalline CB–α-MnO_2 transformed into a more crystalline CB–MnO_2@Zn phase. Similarly, the thermal stability of the CB–α-MnO_2 matrix improved markedly after Zn^{2+} intercalation. Electrochemical analysis of CB–MnO_2 in the presence of dilute Zn^{2+} (1 mM) in 0.1 M KCl showed a distinct redox peak corresponding to the MnO_2/MnOOH transformation, highlighting the specific role of Zn^{2+} in modulating redox activity. This pseudocapacitive behavior led to a significantly enhanced capacitance of 820 F g^{-1} at a current density of 1 A g^{-1}, substantially higher than most reported MnO_2 or carbon–MnO_2 composites, which typically range between 200 and 400 F g^{-1}. The composite also demonstrated excellent cycling stability, retaining substantial performance over ∼5000 charge–discharge cycles. The mechanism of Zn^{2+} intercalation was further investigated using *in situ* electrochemical quartz crystal microbalance (EQCM) and scanning electrochemical microscopy (SECM). These analyses indicated the reversible formation of zinc hydroxysulfate (ZHS) phases along with ZnO/$Zn(OH)_2$ species during potential cycling, supporting the intercalation/deintercalation behavior of Zn^{2+}. SECM imaging provided spatial insight into Zn^{2+} intercalation at the electrode surface. The CB–MnO_2@Zn composite was also tested as a cathode in an aqueous Zn^{2+}/K^+ hybrid ions battery, paired with a Zn metal anode. The system demonstrated excellent anode reversibility and high overpotentials for both oxygen and hydrogen evolution reactions, an advantage for safe, high-voltage operation. Charge/discharge cycling further confirmed Zn^{2+} intercalation, as evidenced by systematic IR spectral shifts observed *via in situ* FTIR spectroscopy. This newly developed aqueous Zn-ions battery exhibited an exceptional capacity of 315 mAh g^{-1} at a high operating voltage of 2.5 V – a record-high value for Zn-ion batteries reported to date. The battery also maintained stable charge–discharge behavior over 5000 cycles with commendable capacity retention and coulombic efficiency. Given its use of low-cost materials, scalable preparation route, and outstanding performance in both supercapacitor and battery modes, the CB–MnO_2@Zn system holds strong promise for future real-world energy storage applications.

Author contributions

The manuscript was written through the contributions of all authors. All authors have given approval to the final version of the manuscript.

Open Access Article. Published on 11 May 2026. Downloaded on 6/1/2026 10:54:30 PM. This article is licensed under a Creative Commons Attribution-NonCommercial 3.0 Unported Licence.

Conflicts of interest

The authors declare no competing financial interest.

Data availability

The data supporting this article have been included as part of the supplementary information (SI). Supplementary information: scheme of synthesis of cathode material; DTA data; FE-SEM EDX data; effect of electrolyte concentration optimization; EQCM and SECM control experiments. See DOI: https://doi.org/10.1039/d5ma01472g.

Acknowledgements

The authors acknowledge the Department of Science and Technology – Science and Engineering Research Board (DST/CRG/2021/001048) scheme for financial support.

References

1 D. Kundu, B. D. Adams, V. Duffort, S. H. Vajargah and L. F. Nazar, *Nat. Energy*, 2016, **1**, 1.

2 Y. You and A. Manthiram, *Adv. Energy Mater.*, 2018, **8**, 1701785.

3 Y. Luo, Z. Rao, X. Yang, C. Wang, X. Sun and X. Li, *Energy Environ. Sci.*, 2024, **17**, 7543.

4 Y. Dai and A. Panahi, *Next Energy*, 2025, **6**, 100186.

5 M. M. Hasan, R. Haque, M. I. Jsahirul, M. G. Rasul, I. M. R. Fattah, N. M. S. Hassan and M. Mofijur, *J. Energy Storage*, 2025, **120**, 116511.

6 J. T. Frith, M. J. Lacey and U. Ulissi, *Nat. Commun.*, 2023, **14**, 420.

7 B. K. Roy, I. Tahmid and T. U. Rashid, *J. Mater. Chem. A.*, 2021, **9**, 17592.

8 A. Ahmed, M. R. Abdul Karim and M. Usman, *Energy Technol.*, 2025, 2401761.

9 M. R. Lukatskaya, B. Dunn and Y. Gogotsi, *Nat. Commun.*, 2016, **7**, 12467.

10 G. G. Amatucci, F. Badway, A. Du Pasquier and T. Zheng, *J. Electrochem. Soc.*, 2001, **148**, A930–A939.

11 T. Kim, W. Song, D.-Y. Son, L. K. Ono and Y. Qi, *J. Mater. Chem. A*, 2019, **7**, 2942–2959.

12 X. Li, M. Li, Q. Yang, H. Li, H. Xu, Z. Chai, K. Chen, Z. Liu, Z. Tang, L. Ma, Z. Huang, B. Dong, X. Yin, Q. Huang and C. Zhi, *ACS Nano*, 2020, **14**, 541.

13 G. H. An, J. Hong, S. Pak, Y. Cho, S. Lee, B. Hou and S. Cha, *Adv. Energy Mater.*, 2019, **10**, 1902981.

14 L. Yu, J. Li, N. Ahmad, X. He, G. Wan, R. Liu, X. Ma, J. Liang, Z. Jiang and G. Zhang, *J. Mater. Chem. A*, 2024, **12**, 9400–9419.

15 Z. Huang, R. Zhang, S. Zhang, P. Li, C. Li and C. Zhi, *Mater. Futures*, 2022, **1**, 022101.

16 X. Han, X. Kong, D. Wang, X. Li and L. Dong, *Chem. Eng. J.*, 2023, **477**, 147078.

17 Z. Fan, J. Jin, C. Li, J. Cai, C. Wei, Y. Shao, G. Zou and J. Sun, *ACS Nano*, 2021, **15**, 3098–3107.

18 Y. Liu, L. Wu, J. Wu and R. Zhang, *J. Energy Storage*, 2025, **136**, 118638.

19 M. Song, H. Tan, D. Chao and H. J. Fan, *Adv. Funct. Mater.*, 2018, **28**, 1802564.

20 X. Lu, M. Yu, G. Wang, Y. Tong and Y. Li, *Energy Environ. Sci.*, 2014, **7**, 2160.

21 X. Zhou, W. Yang, C. Wu, S. Li and L. Li, *Energy Fuels*, 2025, **39**, 9641–9667.

22 Y. G. Lee, G. Yoo, Y. R. Jo, H.-R. An, B. R. Koo and G.-H. An, *Adv. Energy Mater.*, 2023, **13**, 2300630.

23 H. Wang, X. Wang, X. Liu, S. Zhang, S. Meng, W. Yan, X. Zhang, Z. Lu, Z. Qiu, H. Xu and J. He, *J. Alloys Compd.*, 2025, **1020**, 179588.

24 H. Xiao, D. Xiong, B. Lu, Y. Meng, F. Zhang, J. Zhou, J. Zhou, L. Ye, T. Long, J. Yin, Y. Yang, X. Chen and L. Yang, *Inorg. Chem.*, 2025, **64**, 8322–8333.

25 Y. Dong, H. Hu, P. Liang, L. Xue, X. Chai, F. Liu, M. Yu and F. Cheng, *Nat. Rev. Chem.*, 2025, **9**, 102.

26 G. Li, L. Sun, S. Zhang, C. Zhang, H. Jin, K. Davey, G. Liang, S. Liu, J. Mao and Z. Guo, *Adv. Funct. Mater.*, 2024, **34**, 2301291.

27 L. Wu, Z. Li, Y. Xiang, W. Dong, X. Qi, Z. Ling, Y. Xu, H. Wu, M. D. Levi, N. Shpigel and X. Zhang, *Small*, 2024, **20**, 2404583.

28 L. Suo, O. Borodin, T. Gao, M. Olguin, J. Ho, X. Fan, C. Luo, C. Wang and K. Xu, *Science*, 2015, **350**, 938.

29 J. Wang, J. G. Wang, H. Liu, C. Wei and F. Kang, *J. Mater. Chem. A*, 2019, **7**, 13727.

30 G. Fang, C. Zhu, M. Chen, J. Zhou, B. Tang, X. Cao, X. Zheng, A. Pan and S. Liang, *Adv. Funct. Mater.*, 2019, **29**, 1808375.

31 S. Wang, Q. Wang, W. Zeng, M. Wang, L. Ruan and Y. Ma, *Nano-Micro Lett.*, 2019, **11**, 70.

32 J. Zeng, L. Dong, L. Sun, W. Wang, Y. Zhou, L. Wei and X. Guo, *Nano-Micro Lett.*, 2020, **13**, 1.

33 X. Ma, J. Cheng, L. Dong, W. Liu, J. Mou, L. Zhao, J. Wang, D. Ren, J. Wu, C. Xu and F. Kang, *Energy Storage Mater.*, 2019, **20**, 335–342.

34 Y. A. Kumar, J. K. Alagarasan, T. Ramachandran, M. Rezeq, M. A. Bajaber, A. A. Alalwiat, M. Moniruzzaman and M. Lee, *J. Energy Storage*, 2024, **86**, 111119.

35 Y. Anil Kumar, G. Koyyada, T. Ramachandran, J. H. Kim, S. Sajid, M. Moniruzzaman, S. Alzahmi and I. M. Obaidat, *Nanomaterials*, 2023, **13**, 1049.

36 Q. Chen, J. Jin, Z. Kou, C. Liao, Z. Liu, L. Zhou, J. Wang and L. Mai, *Small*, 2020, **16**, 2000091.

37 J. Sun, L. Zhang, F. Li, F. Yang, M. Liu, S. Li and D. Zhang, *Adv. Funct. Mater.*, 2025, **35**, 2501181.

38 S. He, Z. Mo, C. Shuai, W. Liu, R. Yue, G. Liu, H. Pei, Y. Chen, N. Liu and R. Guo, *Appl. Surf. Sci.*, 2022, **577**, 151904.

39 Q. Chen, X. Lou, Y. Yuan, K. You, C. Li, C. Jiang, Y. Zeng, S. Zhou, J. Zhang, G. Hou, J. Lu and Y. Tang, *Adv. Mater.*, 2023, **35**, 2306294.

© 2026 The Author(s). Published by the Royal Society of Chemistry

Open Access Article. Published on 11 May 2026. Downloaded on 6/1/2026 10:54:30 PM.
This article is licensed under a Creative Commons Attribution-NonCommercial 3.0 Unported Licence.

40 C. Liu, V. Martin-Diaconescu, A. P. Black, S. Khabazian, B. Mundet, K. Matlak, L. Stievano, A. Sorrentino, L. Simonelli and D. Tonti, *Energy Environ. Sci.*, 2025, **18**, 9611–9622.

41 C. Xu, B. Li, H. Du and F. Kang, *Angew. Chem., Int. Ed.*, 2012, **51**, 933–935.

42 G. Liu, H. Huang, R. Bi, X. Xiao, T. Ma and L. Zhang, *J. Mater. Chem. A*, 2019, **7**, 20806–20812.

43 C. Guo, L. Ai, R. Ma, L. Yan, X. Ding, C. Leng, D. Jia, M. Xu, N. Guo and L. Wang, *J. Colloid Interface Sci.*, 2023, **646**, 679–686.

44 J. Hao, S. Zhang, H. Wu, L. Yuan, K. Davey and S.-Z. Qiao, *Chem. Soc. Rev.*, 2024, **53**, 4312–4332.

45 Q. Li, K. Ma, C. Hong, Z. Yang, C. Qi, G. Yang and C. Wang, *Energy Storage Mater.*, 2021, **42**, 715–722.

46 Y. Zhang, Y. Liu, Z. Liu, X. Wu, Y. Wen, H. Chen, X. Ni, G. Liu, J. Huang and S. Peng, *J. Energy Chem.*, 2022, **64**, 23–32.

47 J. Wang, J.-G. Wang, H. Liu, C. Wei and F. Kang, *J. Mater. Chem. A*, 2019, **7**, 13727–13735.

48 J. Huang, Z. Wang, M. Hou, X. Dong, Y. Liu, Y. Wang and Y. Xia, *Nat. Commun.*, 2018, **9**, 2906.

49 B. Lee, H. R. Seo, H. R. Lee, C. S. Yoon, J. H. Kim, K. Y. Chung, B. W. Cho and S. H. Oh, *ChemSusChem*, 2016, **9**, 2948–2956.

50 Md Obaidullah, T. Furusawa, I. A. Siddiquey, N. M. Bahadur, M. Sato and N. Suzuki, *Adv. Powder Technol.*, 2018, **29**, 1804.

51 L. Kang, M. Zhang, Z.-H. Liu and K. Ooi, *Spectrochim. Acta, Part A*, 2007, **67**, 864.

52 S. Saikrithika and A. Senthil Kumar, *J. Phys. Chem. C*, 2023, **127**, 8016.

53 D. A. McKeown and J. E. Post, *Am. Mineral.*, 2001, **86**, 701.

54 J. E. Post, D. A. McKeown and P. J. Heaney, *Am. Mineral.*, 2021, **106**, 351.

55 D. Chen, D. Ding, X. Li, G. H. Waller, X. Xiong, M. A. El-Sayed and M. Liu, *Chem. Mater.*, 2015, **27**, 6608.

56 H. Liu, S. Kazemiabnavi, A. Grenier, G. Vaughan, M. Di Michiel, B. J. Polzin, K. Thornton, K. W. Chapman and P. J. Chupas, *ACS Appl. Mater. Interfaces*, 2019, **11**, 18386.

57 Y. C. Tang, G. M. Zhu, Y. L. Kang, L. J. Yue and X. L. Jiao, *J. Alloys Compd.*, 2016, **663**, 784–795.

58 A. C. Ferrari and J. Robertson, *Phys. Rev. B: Condens. Matter Mater. Phys.*, 2000, **61**, 14095.

59 N. Thonglhueng, R. Sirisangsawang, S. Sukpancharoen and N. Phetyim, *Heliyon*, 2022, **8**, e11971.

60 J. Song, M. Liu, X. Ma, Q. Tian, J. Feng, X. Zhong and F. Duan, *J. Alloys Compd.*, 2023, **962**, 171208.

61 G. Rekha, R. Tholkappiyan, K. Vishista and F. Hamed, *Appl. Surf. Sci.*, 2016, **385**, 171–181.

62 J. Bennet, R. Tholkappiyan, K. Vishista, N. V. Jaya and F. Hamed, *Appl. Surf. Sci.*, 2016, **383**, 113–125.

63 R. Tholkappiyan and K. Vishista, *Appl. Surf. Sci.*, 2015, **351**, 1016–1024.

64 E. Alonso, C. Hutter, M. Romero, A. Steinfeld and J. Gonzalez-Aguilar, *Energy Fuels*, 2013, **27**, 4884–4890.

65 E. S. Ilton, J. E. Post, P. J. Heaney, F. T. Ling and S. N. Kerisit, *Appl. Surf. Sci.*, 2016, **366**, 475.

66 M. C. Biesinger, B. P. Payne, A. P. Grosvenor, L. W. M. Lau, A. R. Gerson and R. St. C. Smart, *Appl. Surf. Sci.*, 2011, **257**, 2717.

67 Y. Zhao, R. Zhao, Y. Gao, J. Wang, W. Sun and H. Wang, *J. Alloys Compd.*, 2021, **875**, 160029.

68 R. Rajesh and A. S. Kumar, *Adv. Sustainable Syst.*, 2025, **9**, e00859.

69 H. Chen, C. Dai, F. Xiao, Q. Yang, S. Cai, M. Xu, H. J. Fan and S.-J. Bao, *Adv. Mater.*, 2022, **34**, 2109092.

70 G. Li, W. Yu, Q. Diao, Y. Zhang, F. Tang, X. Luo, L. Yan, X. Zhao and G. Li, *Chem. Phys. Chem.*, 2025, **26**, e202400860.

71 M. Shin, K. P. Sharma, K. Kim, G. P. Awasthi and C. Yu, *J. Phys. Chem. Solids*, 2023, **177**, 111310.

72 Q. Gou, J. Xu, H. Luo, J. Wang, B. Zhang, J. Deng, N. A. N. Ouedraogo, Y. Zheng, S. Lu, J. Xiao, K. Sun and M. Li, *Electrochim. Acta*, 2022, **431**, 141127.

73 T. Xu, K. Yin, J. Gu, Q. Li, Z. Fang, Z. Chen, Y. Wang, N. Qu, S. Li, Z. Xiao and D. Wang, *Langmuir*, 2022, **38**, 12530.

74 H. L. Pan, Y. Y. Shao, P. Yan, Y. Chen, K. S. Han, Z. M. Nie, C. M. Wang, J. Liu, S. X. Wang and J. Xiao, *Nat. Energy*, 2016, **1**, 16039.

75 S. Cui, D. Zhang and Y. Gan, *Adv. Energy Mater.*, 2024, **14**, 2302655.

76 T. Hwang, M. Bergschneider, F. Kong and K. Cho, *Chem. Mater.*, 2025, **37**, 1244.

77 L. Wu, Z. Li, Y. Xiang, W. Dong, X. Qi, Z. Ling, Y. Xu, H. Wu, M. D. Levi, N. Shpigel and X. Zhang, *Small*, 2024, **20**, 2404583.

78 N. Roy, G. Rajasekhara Reddy, M. R. Pallavolu, R. R. Nallapureddy, M. Dhananjaya, A. Sai Kumar, A. N. Banerjee, B.-K. Min, H. R. Barai and S. W. Joo, *ACS Appl. Mater. Interfaces*, 2024, **16**, 34859.

79 J. Li, X. Yang, D. Ma, J. Liu, C. Ma, N. Liu, L. Lu, T. Wang, X. Pang, Y. Yang, Q. Zhang and X. Li, *J. Colloid Interface Sci.*, 2024, **676**, 927.

80 S. Xi, X. Cheng, X. Gao and X. Qian, *ACS Appl. Energy Mater.*, 2024, **7**, 5081.

81 M. M. Mohamed, Y. P. Hardianto, A. Hussain, S. A. Ganiyu, M. A. Gondal and Md. A. Aziz, *Appl. Surf. Sci.*, 2024, **669**, 160472.

82 P. Luo, Z. Huang, W. Zhang, C. Liu, G. Liu, M. Huang, Y. Xiao, H. Luo, Z. Qu, S. Dong, L. Xia, H. Tang and Q. An, *ChemSusChem*, 2022, **15**, e202200706.

83 N. Roy, G. Rajasekhara Reddy, M. R. Pallavolu, R. R. Nallapureddy, M. Dhananjaya, A. Sai Kumar, A. N. Banerjee, B.-K. Min, H. R. Barai and S. W. Joo, *ACS Appl. Mater. Interfaces*, 2024, **16**, 34859.

84 S. Xi, X. Cheng, X. Gao and X. Qian, *ACS Appl. Energy Mater.*, 2024, **7**, 5081.

85 Z. Tian, Z. Zhao, Y. Chen, D. Li, Y. Wang, X. Wang and L. Guo, *J. Alloys Compd.*, 2022, **925**, 166682.

© 2026 The Author(s). Published by the Royal Society of Chemistry